THE UNIVERSITY OF MANITOBA

STUDY OF SOME PHYSICAL ASPECTS OF THE OPTICALLY PUMPED POLARIZED H^- ION SOURCE AND ITS BEAM DYNAMICS.

by

© Martin Wai-Ming Law

B.Sc.(Hons.) King's College, University of London, 1980.

M.Sc. King's College, University of London, 1981.

A THESIS

SUBMITTED TO THE FACULTY OF GRADUATE STUDIES AND RESEARCH IN PARTIAL FULFILMENT OF THE REQUIREMENTS FOR THE DEGREE OF DOCTOR OF PHILOSOPHY

IN

ACCELERATOR PHYSICS

DEPARTMENT OF PHYSICS

WINNIPEG, MANITOBA

FALL, 1988

National Library of Canada
Bibliothèque nationale du Canada

Canadian Theses Service
Service des thèses canadiennes

Ottawa, Canada
K1A 0N4

The author has granted an irrevocable non-exclusive licence allowing the National Library of Canada to reproduce, loan, distribute or sell copies of his/her thesis by any means and in any form or format, making this thesis available to interested persons.

L'auteur a accordé une licence irrévocable et non exclusive permettant à la Bibliothèque nationale du Canada de reproduire, prêter, distribuer ou vendre des copies de sa thèse de quelque manière et sous quelque forme que ce soit pour mettre des exemplaires de cette thèse à la disposition des personnes intéressées.

The author retains ownership of the copyright in his/her thesis. Neither the thesis nor substantial extracts from it may be printed or otherwise reproduced without his/her permission.

L'auteur conserve la propriété du droit d'auteur qui protège sa thèse. Ni la thèse ni des extraits substantiels de celle-ci ne doivent être imprimés ou autrement reproduits sans son autorisation.

ISBN 0-315-51680-1

Canada

STUDY OF SOME PHYSICAL ASPECTS OF THE OPTICALLY PUMPED POLARIZED H^- ION SOURCE AND ITS BEAM DYNAMICS

BY

MARTIN WAI-MING LAW

A thesis submitted to the Faculty of Graduate Studies of
the University of Manitoba in partial fulfillment of the requirements
of the degree of

DOCTOR OF PHILOSOPHY

© 1989

Permission has been granted to the LIBRARY OF THE UNIVERSITY OF MANITOBA to lend or sell copies of this thesis, to the NATIONAL LIBRARY OF CANADA to microfilm this thesis and to lend or sell copies of the film, and UNIVERSITY MICROFILMS to publish an abstract of this thesis.

The author reserves other publication rights, and neither the thesis nor extensive extracts from it may be printed or otherwise reproduced without the author's written permission.

THE UNIVERSITY OF MANITOBA

RELEASE FORM

NAME OF AUTHOR: Martin Wai-Ming Law

TITLE OF THESIS: Study of Some Physical Aspects of The Optically Pumped Polarized H^- Ion Source and Its Beam Dynamics

DEGREE: DOCTOR OF PHILOSOPHY

YEAR THIS DEGREE GRANTED: 1989

Permission is hereby granted to THE UNIVERSITY OF MANITOBA LIBRARY to reproduce single copies of this thesis and to lend or sell such copies for private, scholarly or scientific research purposes only.

The author reserves other publication rights, and neither the thesis nor extensive abstracts from it may be printed or otherwise reproduced without the author's written permission.

(Signed) W. M. Law

PERMANENT ADDRESS:

TRIUMF

4004 Wesbrook Mall

Vancouver, B.C.

CANADA, V6T 2A3

DATED: 3rd April, 1989

Dedication

To my parents

Abstract

A dc optically pumped polarized H^- ion source has been successfully demonstrated at TRIUMF. Some important physical aspects and beam dynamics problems of the source were studied. The $\langle S_z \rangle$ wall relaxation time of optically pumped polarized sodium atoms on stainless steel, copper and dry-film coated walls has been measured as a function of the applied magnetic field. It has been shown that sodium atoms depolarize after approximately four collisions on a copper wall at high magnetic field, whereas they depolarize after one wall collision on a stainless steel surface. A dry-film coated wall is very effective in preventing depolarization, but is rapidly destroyed when the sodium vapour is used as a charge exchange target with the incident ion beam.

The charge neutralization cross section σ_{+0} of H^+ ions in sodium vapour has been examined by using a Faraday rotation method with a tunable dye laser to measure the target thickness. Results show good agreement with recent theoretical calculations, in spite of the fact that there were significant systematic errors in the measurements. However, the use of the Faraday rotation method has proved to be a useful new approach to obtain the target thickness with improved accuracy, hence reducing the errors in σ_{+0}.

Beam dynamics problems were studied and measured for particle beams in different parts of the source. The emittance parameters and brightness of a proton beam, extracted from the ECR (electron cyclotron resonance) ion source, were investigated as a function of the aspect ratio of the extraction electrode system. The method used can be applied to any ion source with immersed flow beam dynamics.

The emittance of the final H^- beam was measured and found to be linearly dependent on the magnetic field of the ionizer, as predicted by theory. The emittance growth of the H^- beam ionized in a solenoid by

charge exchange is mainly due to the defocusing action of the fringing solenoidal field. The emittance of the H^- beam was 0.4π mm-mrad at the 60% contour level of the total beam for a 1.6 kG ionizer field, and is comparable to the acceptance of the TRIUMF cyclotron.

A beamline for transporting a 5 keV H^- ion beam to the injection line of the TRIUMF cyclotron has been computer-designed using the measured H^- beam emittance as an input parameter. There are two electrostatic bends, two einzel lenses and a Wien filter in the beamline, as well as some beam correcting elements.

Acknowledgements

I am particularly grateful to my supervisor Dr. P.W. Schmor for the guidance and support during my thesis work at TRIUMF. I have also received a great deal of technical assistance from P. Chigmaroff, M. McDonald and H. Wyngaarden in the experimental work presented in this thesis. I also wish to thank Dr. C.D.P. Levy who patiently assisted me throughout my thesis work.

Thanks are due to Dr. J. Uegaki for the winter we worked together on the H^- emittance measurements, and to Dr. R.R. Stevens of LAMPF for his advice in the data analysis.

I would also like to thank Prof. R.J. Slobodrian of Laval University, who let me participate in the research and development of the polarized ^3He ion source and encouraged me to undertake my graduate work in the research of new types of polarized ion sources.

Contents

1 Introduction 1

1.1 Overview 1

1.2 Atomic-beam method 2

1.3 Lamb-shift sources 4

1.4 Beam emittance from different polarized ion sources 4

1.5 Principle of OPPIS 6

1.6 Why is OPPIS of current interest ? 9

1.7 Present status of OPPIS 11

1.8 Optical pumping of Na atoms at high magnetic field 12

1.9 Organization of this thesis 14

2 The OPPIS at TRIUMF 15

2.1 General description 15

2.2 ECR proton source 17

2.3 Na polarization and laser system 17

2.4 Polarization transfer efficiency 21

2.5 Ionizer 22

2.6 Transport beamline to the accelerating column 22

2.7 Vacuum system 23

3 Wall Relaxation Measurements **25**

3.1 Overview 25

3.2 Preparation for different wall surfaces 26

3.3 Polarization relaxation measurement 26

3.4 Relaxation results and analysis 32

3.5 Calculation of local magnetic field and correlation time 34

3.6 Summary of the chapter 39

4 σ_{+0} Measurements of $H^+ \longrightarrow H^0$ in Na Vapour **41**

4.1 Overview 41

4.2 Previous experimental setup 42

4.3 Experimental setup for the present work 44

4.4 Results 48

5 Emittance and Brightness Measurements For ECR Ion Source Extraction **51**

5.1 Overview 51

5.2 The beam matrix in TRANSPORT 52

5.3 Beam transport in a solenoidal field 53

5.4 Emittance measuring device 55

5.5 Experimental method 55

5.6 Application and results 57

6 Emittance Growth of H^- Beam From $H^0 \longrightarrow H^-$ In a Solenoid **67**

6.1 Overview 67

6.2 Derivation and justification of $(\triangle\epsilon)$ 68

6.3 Emittance measurement and results 69

7 Beamline Design **76**

7.1 The beamline 76

7.2 Spin rotator design aspects 77

7.2.1 Calculation of the magnetic and electric field strengths 77

7.2.2 Focussing properties of a Wien filter 78

7.3 Einzel lens design aspects 79

8 Initial Commissioning Experience And Future Research On The TRIUMF OPPIS **83**

8.1 Initial commissioning experience 83

8.2 Future research 85

A Derivation of $P(t)$ **92**

List of Tables

3.1 Tabulation of local magnetic field and correlation time for different wall materials. 39

4.1 Tabulation of charge neutralization cross section σ_{+0} for H^+ ions in Na vapour at different energies. 48

5.1 Tabulation of the emittance parameters and the extracted beam current at different aspect ratio for the extraction system at $B = 0.9B_{max}$. 64

5.2 Tabulation of the emittance parameters and the extracted beam current at different aspect ratio for the extraction system at $B = 0.99B_{max}$. 64

List of Figures

1.1 A block diagram showing a conventional atomic beam source. 3

1.2 A block diagram showing a Lamb-shift source 5

1.3 A block diagram of an optically pumped polarized ion source based on the proposal of Anderson. 8

1.4 Optical pumping of sodium atoms with respect to the D_1 transition. 13

2.1 A schematic drawing of the TRIUMF OPPIS installed on the HV terminal. 16

2.2 A schematic arrangement of the laser system employed in the TRIUMF OPPIS. 19

2.3 A schematic showing the pumping and probe laser beams entering the TRIUMF OPPIS. 20

2.4 A schematic diagram showing the vacuum system in the TRIUMF OPPIS installed on the HV terminal. 24

3.1 Experimental arrangement for the wall relaxation measurements. . . 28

3.2 Photomultiplier (PMT) signal when the pump beam was on and off. 30

3.3 Raw relaxation signals from the oscilloscope traces and their transformed polarization relaxation of Na atoms in different target cells. The applied magnetic field was 1.2 T. (a) and (b) dry-film coated wall, inner diameter = 4.8 mm; (c) and (d) copper cell, inner diameter = 4.9 mm; (e) and (f) stainless steel cell, inner diameter = 4.85 mm. 31

3.4 Observed relaxation time T_{obs} as a function of applied magnetic field; (a) dry-film coated wall, (b) copper wall and stainless steel wall. A small correction to T_{obs} has been made accounting for the time resolution of the detecting system. The curves are smooth curves to the data points. 33

3.5 Variation of mean number of non-depolarizing wall collisions N as a function of applied magnetic field for a copper wall. The curve is a smooth curve to the data points. 35

3.6 Applied magnetic field dependence of steady state Na polarization. Laser power = 0.6 W. Open squares: dry-film coating, Na thickness = 3.8×10^{13} atoms cm^{-2}; solid squares: copper wall, Na thickness = 3.2×10^{13} atoms cm^{-2}; open circles: stainless steel, Na thickness = 3.2×10^{13} atoms cm^{-2}. 36

4.1 A schematic diagram showing the apparatus used by Anderson et al for the charge neutralization cross section measurements for $H^+ \longrightarrow H^0$ in Na vapour. 43

4.2 Experimental setup for the charge neutralization cross section measurements for $H^+ \longrightarrow H^0$ in sodium vapour, using the Faraday rotation method to measure the Na thickness. 45

4.3 Semi-logarithmic plot of (I/I_+) against target thickness nl for a 5 keV H^+ beam. circle: data before the correction for H^- current. cross: data after correction for H^- current. The straight line was fitted for data up to the target thickness of 25×10^{13} atoms cm^{-2} after the correction for H^- current. 47

4.4 A schematic diagram of the proposed σ_{+0} experimental arrangement using an analysing magnet and particle identification detectors. . . . 50

5.1 A schematic diagram of the emittance device. P: rotary probe with seven wires; B: beam stop. 56

5.2 Dimensions of the extraction electrodes system used in the present work. The thickness of the electrodes $D = 0.8$ mm; the gap between electrodes $d = 3.0$ mm; the aperture radii of the electrodes r were varied from 0.5 mm to 1.75 mm. The aspect ratio $S = r/d$. 58

5.3 A schematic diagram showing the experimental setup. S1 and S2: solenoids; ECR: electron-cyclotron-resonance ion source; WG: waveguide for the ECR source; L: extraction electrodes; P: rotary probe; B: beam stop; G: gear to rotate the probe. 59

5.4 (a) An example of a beam profile scan recorded with a X-Y chart recorder. (b) The corresponding half-width of the beam envelope as a function of z/ρ; the solid curve is a cubic-spline fit to the measured x_{max} in data points; the broken curve is a least-squares fit to eq.(5.5). 61

5.5 Phase space ellipses at the extractor for different aspect ratio S. Ellipses with solid curve: extraction system at $B = 0.9B_{max}$; ellipses with broken curve: extraction system at $B = 0.99B_{max}$. 63

5.6 (a) and (b) Measured ϵ_n/S and B_n as a function of S for the extraction system located at $B = 0.9B_{max}$. (c) and (d) Measured ϵ_n/S and B_n as a function of S for the extraction system located at $B = 0.99B_{max}$. The curves are the smooth curves to the data points. 66

6.1 A schematic diagram showing the TRIUMF OPPIS and the position of the Los Alamos slit scanner used in the measurements of the emittance of the H^- beam. The magnetic field profile along the beam axis is shown in the lower part of the diagram. 70

6.2 A schematic diagram showing the Los Alamos type slit scanner and a H^- ion trajectory through the scanner. 71

6.3 Emittance contours for the H^- beam with 0.1 T ionizer field. Contour labels represent the percentage of the total beam within the contours. 73

6.4 Measured normalized emittance of H^- beam as a function of the ionizer magnetic field at a 60% contour level of the total beam. The straight line is the least-squares fit to the data points. 74

7.1 The geometry of the einzel lens used in the transport beamline of the OPPIS at TRIUMF, showing full scale of the lens. 80

7.2 Variation of the focal length of the einzel lens for a 5 keV H^- beam as a function of r_0 at different biasing potentials. 82

8.1 (a) The nuclear polarization of the proton beam at 290 MeV (open squares) and the sodium atomic polarization (solid squares) as a function of sodium thickness. (b) The solid curve is a least-squares fit for the ratio (triangles) of the proton polarization to the sodium atomic polarization. 84

8.2 Beam current as a function of time following spin flip. The energy of the proton beam was 290 MeV. 86

A.1 Example of a photomultiplier (PMT) signal. 94

Chapter 1

Introduction

1.1 Overview

Spin polarized proton beams have been used in many precise polarization measurements and particularly in recent experimental programs studying the possible violation of some of the fundamental symmetry laws. In many recent proposals for high energy accelerators, the acceleration of polarized proton beams also forms a central part of the projects [1,2]. Therefore it is necessary to develop improved ion sources to produce more intense polarized ion beams for such accelerators. Here, discussion is restricted to schemes suitable for producing intense beams of polarized H^- ions.

Existing polarized H^- ion sources can be grouped into three types, namely the atomic beam source, Lamb-shift source and, recently, the optically pumped source. Atomic beam and Lamb-shift sources have been developed and the physical limitations on these types of sources have been studied [3,4], whereas it is only recently that research and development have been undertaken at several laboratories in order to make the optically pumped source operational.

This thesis will report on some important physical aspects and beam dynamics studies in the research and development leading to the successful operation of the

Optically Pumped Polarized H^- Ion Source (OPPIS) at TRIUMF.

In the following sections of this chapter, the schemes for producing intense beams of polarized H^- ions using atomic beam and Lamb-shift sources are only briefly outlined, as the fundamental principles of these sources can be found in review articles [3,4]. Then the principle of OPPIS and its attractive features are discussed in order to see why the development of OPPIS is of current interest, followed by a section on the present status of OPPIS. The physics of optical pumping of Na atoms in a strong magnetic field is presented in section 1.7.

1.2 Atomic-beam method

In a conventional atomic beam source, a dissociator, nozzle and skimmer are used to produce a thermal collimated atomic hydrogen beam. The selection of the electron spin polarization of the atomic beam is achieved by Stern-Gerlach type separation magnets. The electron spin polarized atomic beam is then exposed to an RF field in order to produce transitions from one of the two occupied hyperfine states to another state of opposite electron (and nuclear) spin. After the RF unit, an electron ionizer is used to produce nuclearly polarized H^+ ions, followed by an alkali vapour target if H^- is desired. Alternatively, H^- is also produced directly with the charge exchange reaction $H^0 + Cs \longrightarrow H^- + Cs^+$. The H^- current from the best sources is $\sim$30 μA dc. Although the beam emittance from an atomic beam source depends on the ionization technique, the normalized emittance is about 0.5π mm-mrad for maximum current operation. A block diagram for a conventional atomic beam source is shown in fig. 1.1. The atomic beam source has the potential for substantially higher current, but a great deal of development effort is required to reach the mA current range.

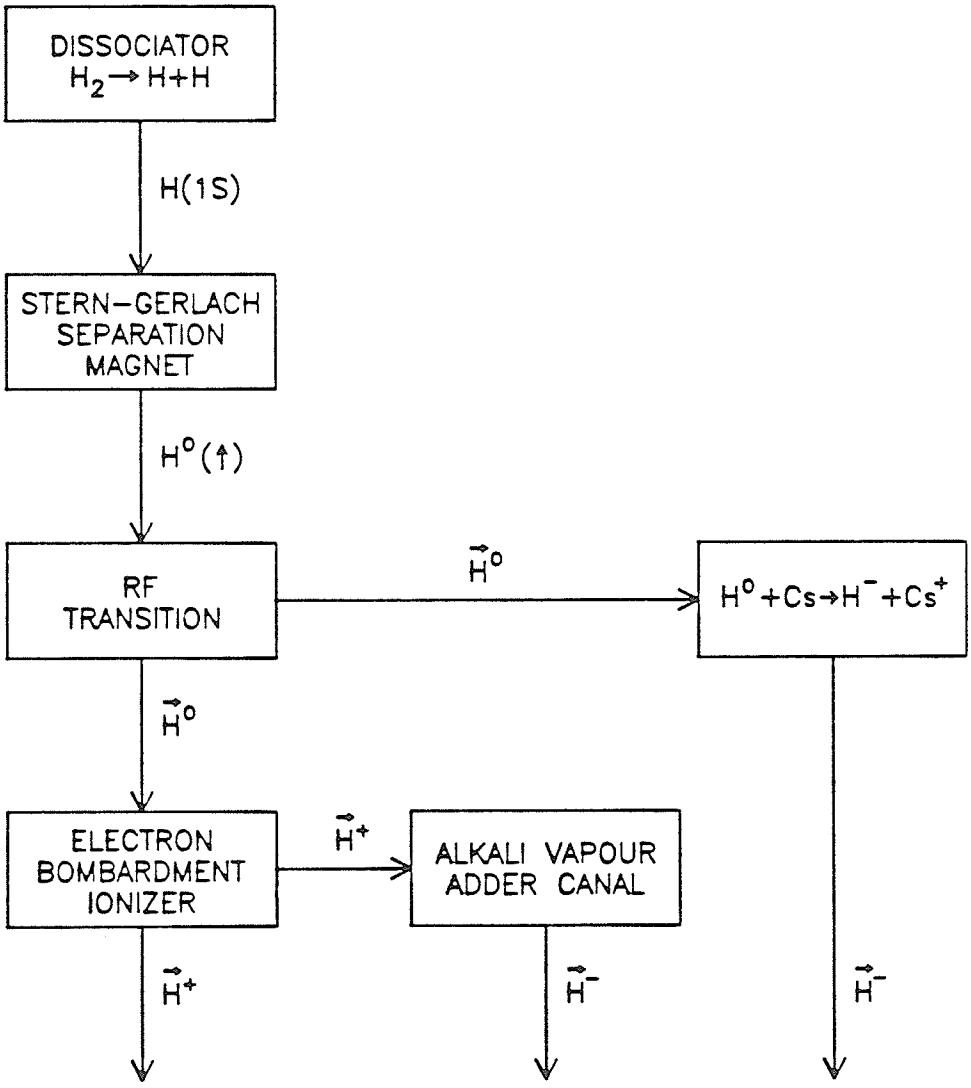

Figure 1.1: A block diagram showing a conventional atomic beam source.

1.3 Lamb-shift sources

Figure 1.2 shows a block diagram outlining the important processes in a Lamb-shift source. A beam of 550 eV H^+ is injected into a Cs charge exchange vapour ($nl \simeq 3{\times}10^{14}$ atoms cm^{-2}) to produce a H(2S) metastable atomic beam. The H(2S) metastable atoms then enter an axial magnetic field of approximately 0.057 T which is appropriate to cause level crossing of the $H(2S_{1/2})$ and $H(2P_{1/2})$ levels. The correct choice and configuration of this magnetic field and of d.c. and r.f. electric fields imposed on the beam while inside the magnetic field cause selective decay of the unwanted H(2S) hyperfine states via mixing with the H(2P) hyperfine states. The remaining H(2S) beam is thus nuclearly polarized. Selective ionization of the polarized H(2S) atoms, preferentially over unpolarized H(1S) atoms in the beam, is accomplished via charge exchange in argon gas to produce nuclearly polarized H^- ions or in iodine to produce nuclearly polarized H^+ ions. The H^- current from the best source has increased to $\sim$2 μA within a normalized emittance of 0.35π mm-mrad. The Lamb-shift sources are reliable to operate, but H^- beam intensities are no longer competitive with other methods.

1.4 Beam emittance from different polarized ion sources

The measure of beam quality which is of importance in ion sources used in particle accelerators is the normalized transverse beam emittance. Ref [5] gives a detailed definition of the concept of emittance. For a brief introduction, the transverse beam emittance is commonly defined as the $x - x'$ or the $y - y'$ phase space area, occupied by the beam particles, where $x' = v_x/v_z$ and $y' = v_y/v_z$ are the angles of divergence in the transverse x and y directions respectively, and v_x, v_y and v_z are the beam velocities in the x, y and z directions respectively. The phase space area is often normalized by multiplying by the relativistic factors β and γ of the beam.

In the operation of polarized H^- ion sources, ionization of a beam of nuclearly

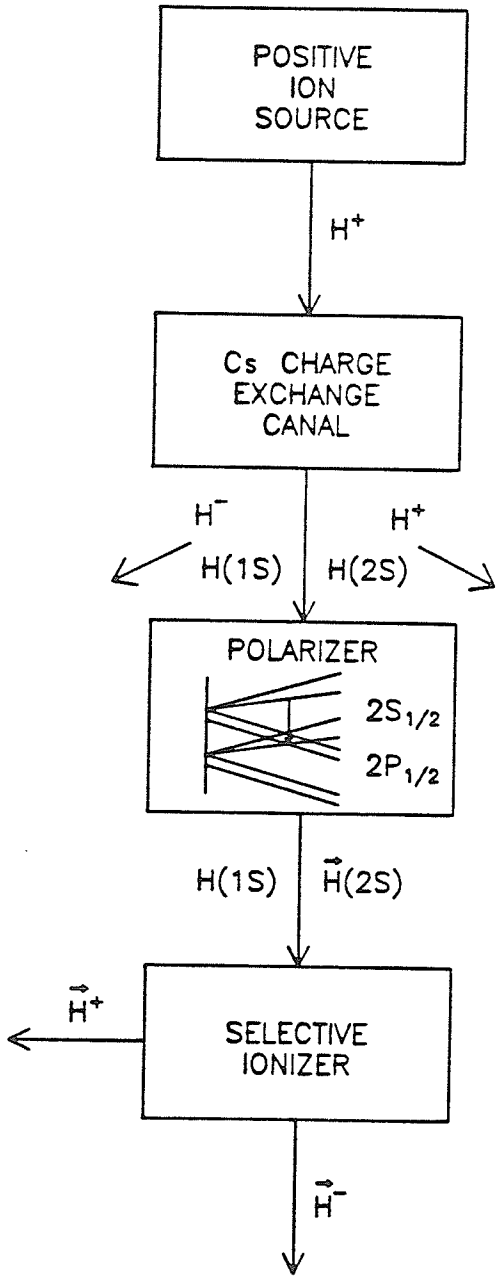

Figure 1.2: A block diagram showing a Lamb-shift source

polarized H^0 neutrals is carried out in an axial magnetic field in order to preserve the nuclear polarization. Ohlsen et al. [6] have predicted that emittance growth occurs when the atomic beam is ionized in a magnetic field. As the trajectories for off-axis H^- particles are defocussed by the radial component B_r in the fringe field of the solenoid, a significant divergence is imparted to the beam. Although there is no increase in the volume of the 4-D (x, x', y, y') transverse phase space occupied by the beam particles (Liouville's Theorem), there is an increase in the projection of this hyper-volume on the $x - x'$ or $y - y'$ transverse phase space plane; this constitutes an effective emittance growth.

As discussed by Ohlsen et al. [6], the emittance growth increases with the strength of the solenoidal field in which ionization takes place. Thus emittance growth is more serious in the strong solenoidal fields used in the electron bombardment ionizer and alkali metal vapour charge exchange region in atomic beam sources than in the much weaker fields used in the argon gas cell in Lamb-shift sources. The emittance growth of the H^- beam produced by an optically pumped source has been investigated and will be presented in chapter 6 of this thesis.

1.5 Principle of OPPIS

A new method of producing polarized ions involves the passage of a beam of ions through an electron spin polarized target where some of the ions pick up polarized electrons. The first proposal of this new method was by Zavoiskii [7] who suggested the production of H^- ions by passing a beam of H^+ (unpolarized) through a ferromagnetic foil magnetized to saturation. Some of the H^+ ions capture polarized electrons forming fast H^0 atoms, which then pass through a weak magnetic field region where the hydrogen nucleus is polarized through hyperfine coupling with the polarized electron. Finally the fast atoms pass through a second foil to form H^- or H^+ ions.

Haeberli [8] improved Zavoiskii's idea by suggesting the use either of a storage vessel with electron polarized H^0 neutrals or of an optically pumped alkali vapour as the charge exchange target.

Witteveen [9] constructed a prototype polarized H^- ion source based on the atomic beam technique with a sextupole magnet to produce a thermal beam of electron spin polarized Na atoms as a charge exchange target for the incident 5 keV H^+ beam. Some of the H^+ ions picked up polarized electrons to form H^0 atoms. The H^0 nuclei were then polarized in a weak magnetic field via hyperfine interaction. The nuclearly polarized H^0 neutrals subsequently passed through a second (unpolarized) Na cell, where the neutrals were partially converted into polarized H^- ions. Although Witteveen's ion source produced a low intensity H^- beam with poor polarization, it demonstrated that nuclearly polarized H^- ions can be produced via the use of an atomic polarized alkali vapour as the charge exchange target as suggested by Haeberli [8].

In 1979, Anderson [10] proposed a technique based on the optical pumping of Na atoms with dye lasers to obtain intense polarized H^- currents. It is here called the Optically Pumped Polarized Ion Source (OPPIS). A block diagram of an OPPIS based on the proposal of Anderson is illustrated in fig. 1.3. This technique involves polarizing the electron spin of Na atoms in an optically thick Na vapour ($nl \geq 10^{13}$ atoms cm^{-2}) by optical pumping with a dye laser tuned to the Na D_1 wavelength (see section 1.8). An H^+ beam, extracted from a proton ion source at 5 keV, is incident on the Na vapour target, in which some of the H^+ ions are neutralized according to the reaction $H^+ + Na(\uparrow) \longrightarrow H^0(\uparrow) + Na^+$, where the vertical arrows indicate the transfer of the electron spin polarization from the sodium atoms to the H^0 neutrals. The fast H^0 atoms emerge from the first Na target and then enter a second (unpolarized) Na vapour target. The magnetic field at the second target is aligned opposite to the field in the first target. The electron spin polarized H^0 atoms pass through a region of near zero magnetic field between the two targets. This is known as the Sona zero crossing [11] which transfers the electron spin polarization of

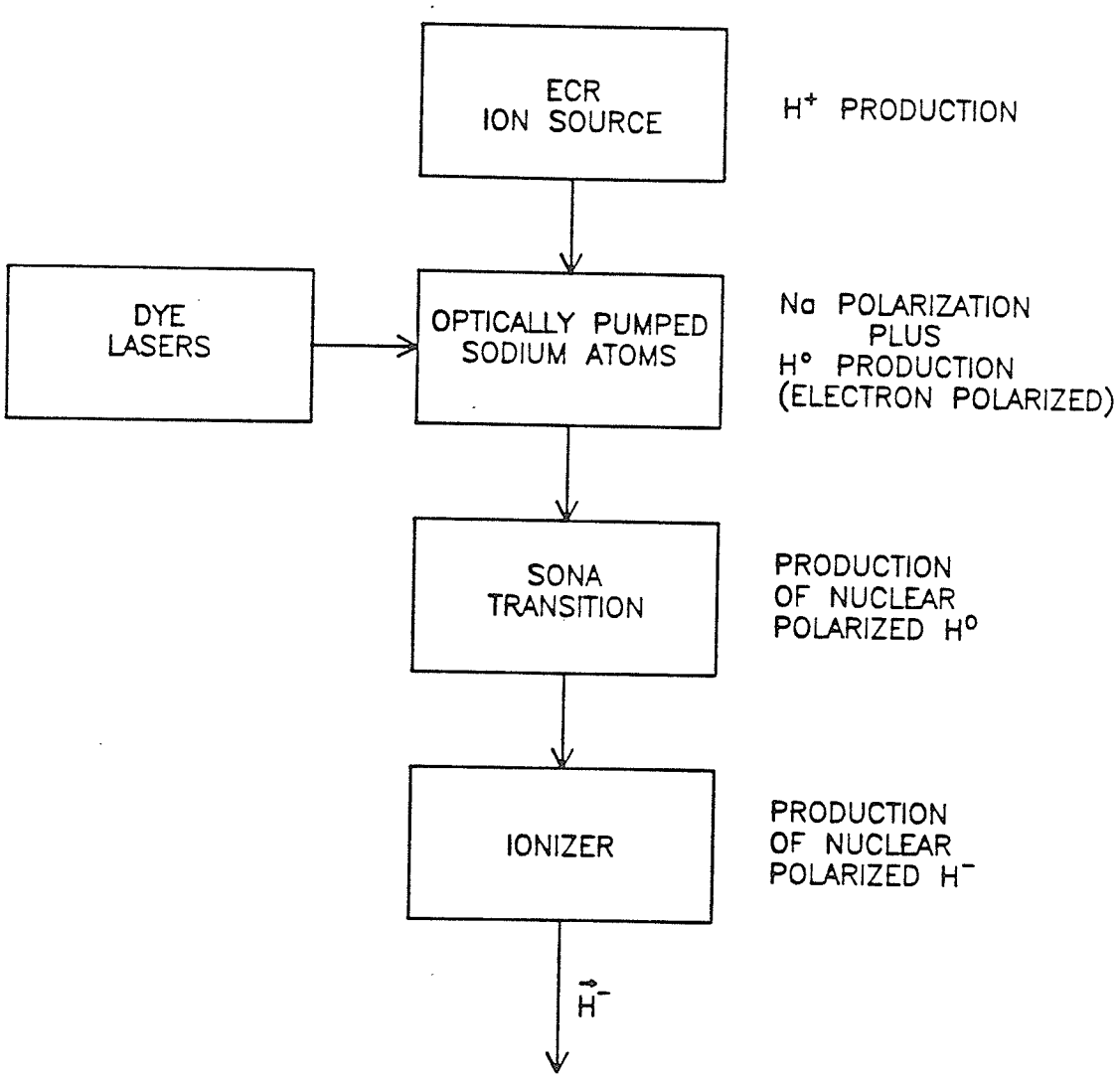

Figure 1.3: A block diagram of an optically pumped polarized ion source based on the proposal of Anderson.

the H^0 atoms to the nuclear polarization. Charge exchange in the second Na vapour within the reversed magnetic field, which is strong enough to decouple the electron and nuclear spins, yields a nuclearly polarized H^- beam. The nuclear polarization of the H^- beam is determined by how effectively the first sodium vapour can be polarized by laser optical pumping, the polarization transfer efficiency, and the effectiveness of the Sona zero crossing. The current of the nuclearly polarized H^- beam depends on the brightness of the initial proton beam, the beam emittance and the maximum sodium target thickness that can be reasonably polarized.

1.6 Why is OPPIS of current interest ?

The reason that an OPPIS has the potential to produce higher polarized H^- current than the atomic beam and Lamb-shift sources can be understood from the following estimate on the potential H^- ion current [10]. A 1 W dye laser operating at the D_1 wavelength of Na (589.6 nm) produces 3×10^{18} photons/sec. At a high magnetic field, in which the nuclear and electron spins of Na atoms are decoupled, 1.5 photons are required on the average to polarize a Na atom. Therefore, 2×10^{18} atoms can be polarized per second. The average time between wall collisions is about 10^{-5} sec, assuming the target cell is a long tube about 10 mm in inner diameter. Even if the Na atoms are completely depolarized at each wall collision, 2×10^{13} Na atoms can be polarized. The long target tube assures that little polarization is lost by effusion of polarized atoms out of the ends of the tube. The charge exchange cross section for the reaction $H^+ + Na \longrightarrow H^0 + Na^+$ at 5 keV is about 4.5×10^{-15} cm^2 (see chapter 4). Thus 9% of the H^+ ions emerge as H^0 neutrals from the first target. The equilibrium fraction of H^- ions emerging from the second Na target is 7.3% [12]. Therefore the estimated current, neglecting aperture restrictions, is about 6 μA of H^- ions per mA of H^+ ions incident on the first Na target with thickness of 2×10^{13} atoms cm^{-2}. As intense H^+ ion sources with tens of mA of proton current output are readily available, it should be possible to produce H^- currents from an OPPIS

much higher than the H^- currents currently produced by atomic beam sources or Lamb-shift sources.

As pointed out by Anderson [10], the reaction $H^+ + Na \longrightarrow H^0 + Na^+$ is nearly resonant for the formation of H^0 atoms in the n=2 level. The electron capture leading to the formation of H^0 atoms in the n=2 level has serious implications for the nuclear polarization of the H^- ions produced by OPPIS. The electron spin polarization of the H^0 atoms is partially lost in the radiative decay to the ground level. However, the loss can be avoided by the use of a strong magnetic field at the first Na target to decouple the $\mathbf{L}$ and $\mathbf{S}$ in the n=2 level of the H^0 atoms (the critical field to decouple $\mathbf{L}$ and $\mathbf{S}$ in the H(n=2) is ~0.35 T). Therefore, the electron spin polarization of the H^0 atoms after decay to the n=1 level is equal to the polarization transferred from the Na atoms.

The nuclear polarization of the H^- beam can be estimated by the product of the atomic polarization of the Na atoms achieved by laser optical pumping, the efficiency of transferring the polarization from Na atoms to the H^0 neutrals, and the effectiveness of the Sona zero crossing. Experimental results on the $\langle S_z \rangle$ wall relaxation time of optically pumped Na atoms show that Na atoms, in a copper cell of inner diameter 4 mm, can be 80% polarized at a thickness of $\sim 4 \times 10^{13}$ atoms cm^{-2} in a 1.2 T magnetic field by a 0.6 W laser beam (chapter 3 of this thesis). The polarization transfer efficiency from Na atoms to the H^0 neutrals was found to be 62% [13]. Assuming that the effectiveness of the Sona zero crossing is 100%, the nuclear polarization of the H^- beam can be therefore as high as 50%. Increasing the nuclear polarization is possible with the use of a more powerful laser beam to increase the Na atomic polarization and of a higher magnetic field in the first Na target to increase the polarization transfer efficiency [14].

The emittance of the H^- beam produced by an OPPIS should be less than the accelerator acceptance, so that most of the H^- beam can be accepted for acceleration. The emittance growth of the H^- beam produced by OPPIS depends on the

strength of the magnetic field in the $H^0 \longrightarrow H^-$ charge exchange region. It is one of the research topics of this thesis to measure the emittance of the H^- beam and to observe the emittance growth as a function of the strength of the magnetic field, and hence to develop an optimum design for the geometry of the charge exchange cell and for the beam transport optics.

Attractive features of OPPIS, when compared with the atomic beam and Lamb-shift sources, are :

- polarization of the hydrogen atomic beam is directly produced and does not rely on quenching or removing undesired substates, potentially resulting in a polarized H^0 beam with less unpolarized background.

- high H^- beam intensity mainly limited by laser power; higher laser power will polarize a higher thickness of Na atoms, increasing the fraction of polarized H^0 neutrals, which are then ionized to H^- ions.

- rapid spin reversal of the nuclear polarization of the H^- beam simply by reversing the helicity of the laser beam without changing the beam energy, current or emittance, so that the acceleration of the H^- beam will not be affected by the spin reversal.

1.7 Present status of OPPIS

The first OPPIS, built at KEK in Japan, has already been used to provide a polarized pulsed beam for the KEK proton synchrotron. Pulsed at a repetition rate 20 Hz with a pulse width of $\sim$70 μsec, the OPPIS at KEK has produced an H^- peak beam current of 50 μA with a nuclear polarization of 56%. At the INR in Moscow, a system containing a duoplasmatron and a neutralizing gas cell replaces the proton source shown in fig. 1.3. Neutral hydrogen atoms at 5 keV are then brought into the magnetic field surrounding the sodium target where the atoms are re-ionized in a

helium gas target prior to picking up polarized electrons from optically pumped Na atoms. The source has been tested both as an H^+ and as an H^- polarized ion source. A polarized H^+ beam of 1 mA with a polarization of 65% has been reported, while a polarized H^- beam of 60 μA with about the same polarization has been achieved. At TRIUMF, a dc H^- source has successfully injected polarized beam into the cyclotron, and has reached a 10 μA beam intensity and ~50% nuclear polarization. A fourth source, which produces a pulsed H^- beam, is in the development stage at LAMPF.

1.8 Optical pumping of Na atoms at high magnetic field

The aim of optical pumping is to create a non-thermal distribution among the different magnetic sublevels belonging to the atomic ground state. The basic principle of optical pumping may be understood with the D_1 transition ($^2S_{1/2}$ to $^2P_{1/2}$) in Na as shown in fig. 1.4. At a high magnetic field (> 1 kG) the total electron angular momentum **J** and the nuclear spin **I** become decoupled and thus m_J and m_I become good quantum numbers. Each of the $^2S_{1/2}$ and $^2P_{1/2}$ atomic states splits into two $m_J = \pm\frac{1}{2}$ substates, each consisting of closely spaced hyperfine levels with $m_I = \frac{3}{2}, \frac{1}{2}, -\frac{1}{2}, -\frac{3}{2}$. The hyperfine splitting in the $^2S_{1/2}$ state is $\delta\nu_{hfs} = 1.76$ GHz. The Doppler width for the D_1 absorption in Na is $\delta\nu_d = 1.7$ GHz at 240°C. In order to optically pump Na atoms in a high magnetic field, it is neccessary for the laser light to interact with the Na atoms in all 4 hyperfine sublevels in the $m_J = -\frac{1}{2}$ belonging to the $^2S_{1/2}$ state and with the Doppler width for the absorption. Thus the laser light must interact with atoms having a distribution of absorption frequencies with a width of about $\delta\nu = \frac{3}{4}\delta\nu_{hfs} + \delta\nu_d \approx 3.0$ GHz. If left-hand circularly polarized (σ^+) light is tuned to the D_1 wavelength, only the transition $\Delta m_J = +1$ is allowed. The atoms in the excited state rapidly ($\tau = 16$ nsec) decay to the ground state, with relative probability η shown in fig. 1.4. Because pumping of the $m_J = -\frac{1}{2}$ substate

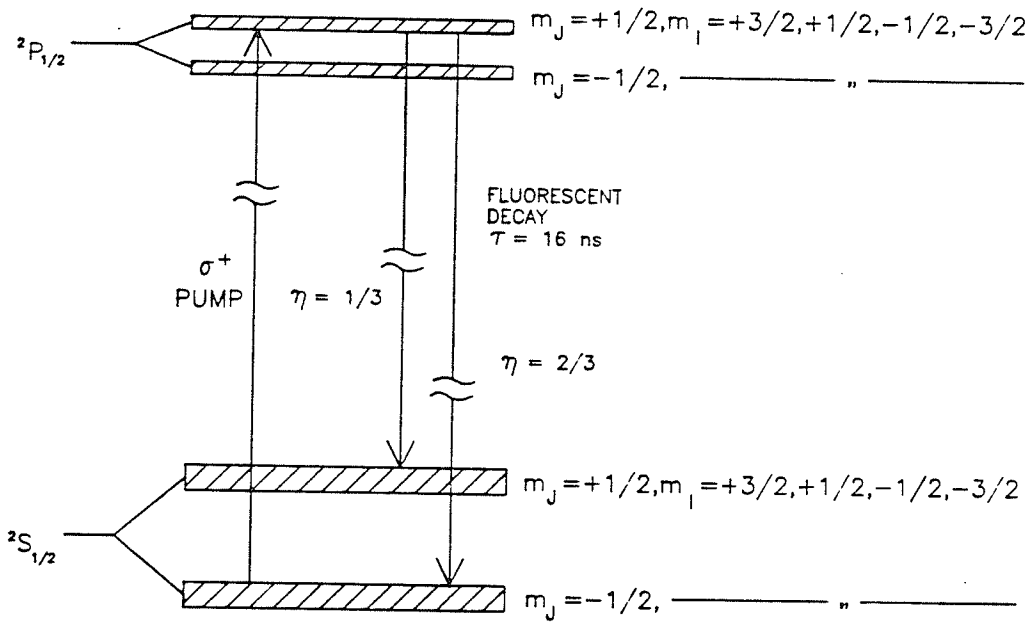

Figure 1.4: Optical pumping of sodium atoms with respect to the D_1 transition.

continues, it is eventually emptied in the absence of mixing between the two $^2S_{1/2}$ substates, leaving all atoms in the $m_J = +\frac{1}{2}$ substate, and thus 100% electron spin polarized.

1.9 Organization of this thesis

Chapter 2 describes the general design and development details of the OPPIS at TRIUMF. It gives some background and the motivation for the research results to be presented in the following chapters. Chapter 3 covers the details of the investigation and measurement of the $\langle S_z \rangle$ wall relaxation of sodium atoms on different wall materials. A suitable wall material for sodium vapour must have a low $\langle S_z \rangle$ relaxation rate and low vapour pressure and must not react with Na at ~300°C. Chapter 4 will discuss the use of a Faraday rotation method to obtain the target thickness in the measurement of the charge neutralization cross section σ_{+0} of H^+ ions in sodium. This approach improves the accuracy of the thickness measurement, and hence yields improved accuracy in the determination of σ_{+0}, which is an important parameter in OPPIS to determine the percentage of incident H^+ ions being neutralized. Chapter 5 presents the mathematical formalism and experimental design of a new method to obtain the emittance parameters and brightness of a H^+ beam extracted from an electron-cyclotron-resonance ion source. This method is used to optimize the geometry of the extracting electrodes for a high brightness H^+ beam and can be applied to ion sources with immersed flow beam dynamics. The interpretation of the results for the emittance measurement of the final H^- beam is the subject of chapter 6. The emittance value of the H^- beam has been used as an input parameter in the design of a low energy beamline to transport the H^- beam to the 300 kV accelerating column. Results on the optical properties of some focussing elements are presented in chapter 7. Future research to improve the beam intensity and polarization of the source will be discussed in chapter 8.

Chapter 2

The OPPIS at TRIUMF

2.1 General description

Since 1977, TRIUMF has been using a Lamb-shift source, which is presently capable of producing up to 1 μA of 75% polarized protons on target. This current is barely adequate for a number of approved experiments. An OPPIS has been under development for the TRIUMF cyclotron since 1983. This has produced an intense dc H^- beam of $\sim$10 μA at a polarization of $\sim$50% from the source and with an emittance suitable for injection into the cyclotron. Approximately 50% of the ion source current can be accelerated to full energy in the cyclotron.

In principle, the TRIUMF OPPIS follows the proposal of Anderson [10] (section 1.5), and its layout is shown in fig. 2.1. A beam of 5 keV protons, extracted from an electron-cyclotron-resonance (ECR) proton source, passes through an optically pumped Na vapour (neutralizer). Polarized electrons are picked up by charge exchange, forming a beam of neutral electron spin polarized hydrogen atoms. An electrostatic field placed in the low field Sona zero crossing [11] region remove charged particles exiting the Na neutralizer. The H^0 neutrals are ionized to H^- ions in a second charge exchange Na cell (negative ionizer) located in the reversed field of 0.2 T. The transport of the H^- beam to the 300 kV accelerating column is carried out

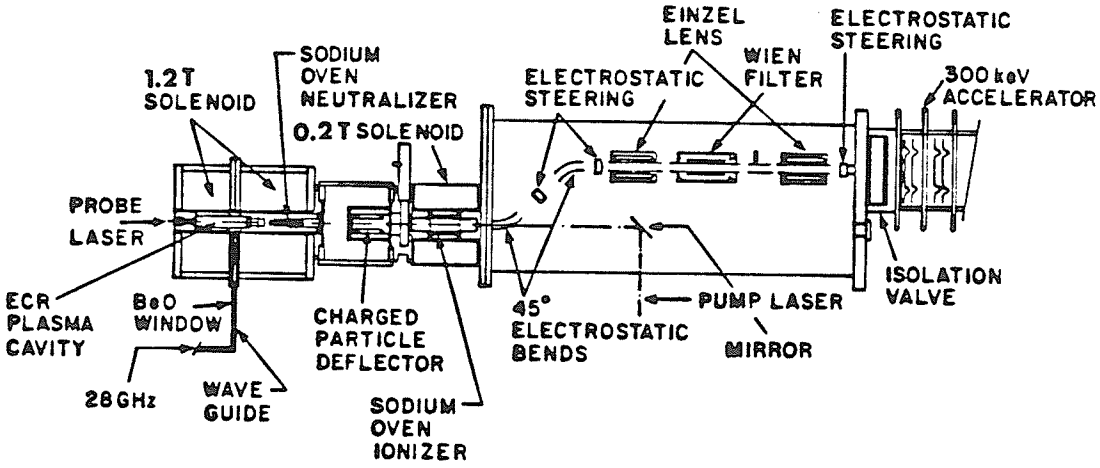

Figure 2.1: A schematic drawing of the TRIUMF OPPIS installed on the HV terminal.

by a series of electrostatic focussing elements. A beamline extension has been built to connect this terminal to the existing cyclotron injection beamline.

The OPPIS is now capable of producing a dc beam of ~10 μA of H^- ions of ~50% polarization and within a normalized emittance of 0.4π mm-mrad. The TRIUMF OPPIS is the only existing dc optically pumped polarized H^- source.

In the following sections, important parts and operating conditions of the source are described. Research areas, of which results are presented in this thesis, are also pointed out.

2.2 ECR proton source

A hydrogen plasma is produced in a multi-mode ECR cavity by up to 600 W absorbed cw microwave power at 28 GHz from a Varian extended interaction oscillator (model VKQ-2H35F). With a quartz liner in the ECR cavity the proton ratio $[H^+/(H^+ + H_2^+ + H_3^+)]$ is greater than 75%. The extraction electrodes and the Na neutralizing cell are located in a ~1.2 T axial magnetic field. The field has a mirror configuration with a minimum at 0.8 T, where the hydrogen gas and microwave power are fed in radially through the waveguide. The H^+ current, extracted at an energy of 5 keV from the water-cooled acceleration-deceleration type multi-aperture (9 apertures of 2 mm diameter each) molybdenum electrodes, can routinely reach 50 mA. The geometry of the extracting electrodes has been investigated in order to extract a high brightness H^+ beam from the ECR source.

2.3 Na polarization and laser system

The Na atoms in the neutralizer are polarized by circularly polarized light tuned to the D_1 wavelength of Na at 589.6 nm. The polarization of the atoms depends on the polarization rate due to optical pumping and the depolarization rates due to

wall relaxation, effusion of polarized atoms out of the neutralizer cell, and at higher target thickness, radiation trapping [15]. The Na cell was 66 mm in length with water-cooled baffles at both ends of the cell to confine the vapour. Wall relaxation of the longitudinal electron spin observable $\langle S_z \rangle$ of optically pumped Na atoms on copper, 'dry-film' and stainless steel surfaces has been measured as a function of the applied magnetic field and will be discussed in chapter 3.

With the TRIUMF OPPIS mounted in a 300 kV terminal of the cyclotron, the laser system (fig. 2.2) used to polarize and monitor the target thickness and polarization of the Na target is located in a room at ground potential. In normal operation, three laser beams of total power $\sim$2 W from three Coherent CR-590 broadband dye lasers are used to optically pump the Na vapour. Narrowing the bandwidth of each pumping beam from a nominal 30 GHz to $\sim$6 GHz with an uncoated 0.5 mm thick intra-cavity etalon increases the spectral power density of the laser light within the 3 GHz Doppler width of the Na D_1 transition. The beams from the three pumping lasers combine with each other to form a single pumping beam before going through a Pockels cell, in which the helicity of the pumping beam may be flipped at rates up to 100 Hz by applying an external voltage. A beam of linearly polarized light, emitted by a fourth dye laser of the same type, at 589.3 nm midway between the two Na D lines, is used to measure the thickness and atomic polarization of the Na vapour. The wavelengths of these four laser beams can be individually monitored with a wavemeter and their spectral properties can be measured with a spectrum analyser. A set of functional requirements to computerize the laser system has been designed and both hardware and software developments are being implemented to the laser system.

The pumping beam polarizes the Na vapour from the downstream direction of the source, while the probe beam enters the source from upstream (fig. 2.3). The probe beam is brought by a fibre optic back to the laser room, where the thickness and polarization measurements on the Na vapour are made. As seen in fig. 2.3, a $\sim$20 cm long cell filled with argon gas at a pressure of about 30 mTorr is used for

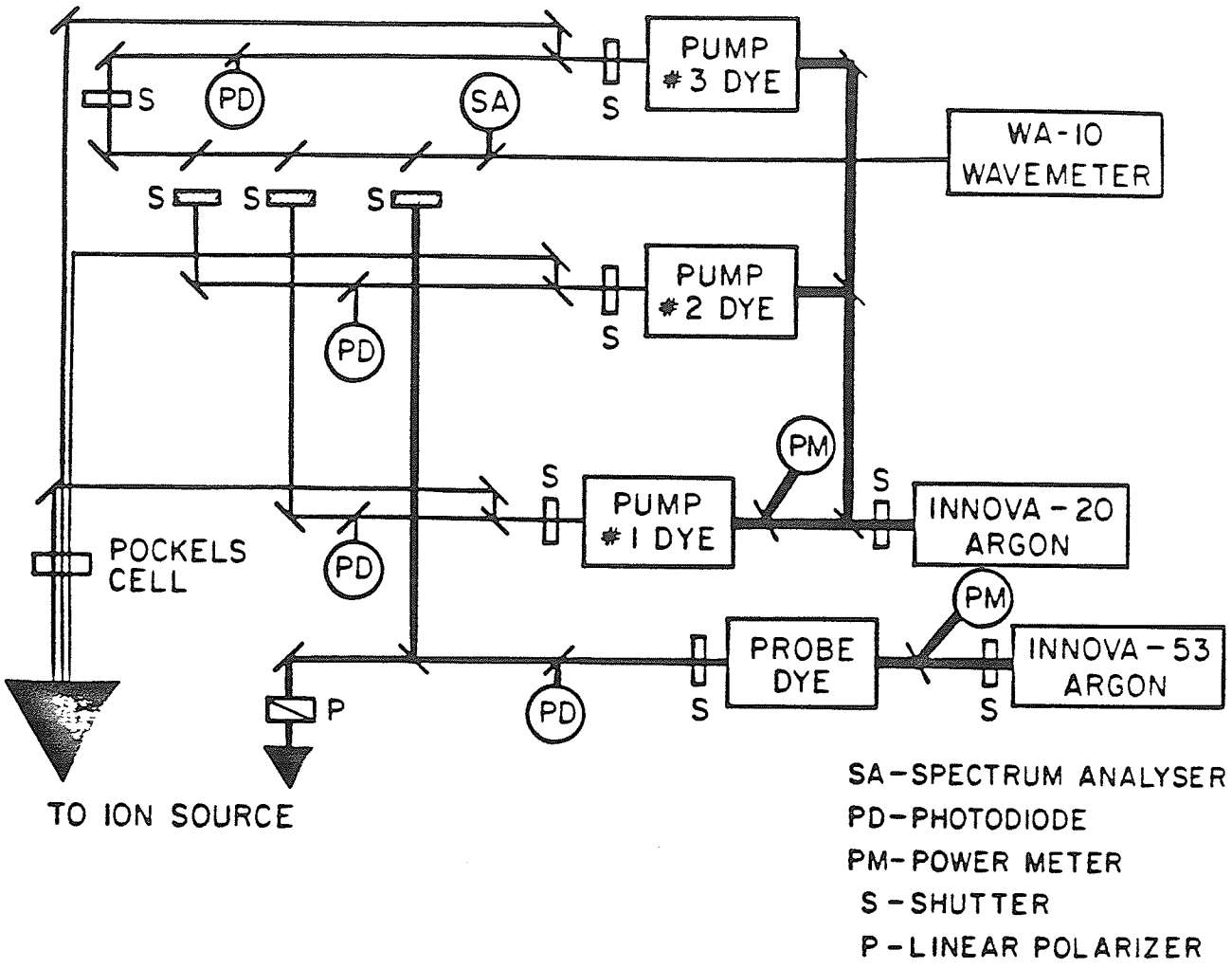

Figure 2.2: A schematic arrangement of the laser system employed in the TRIUMF OPPIS.

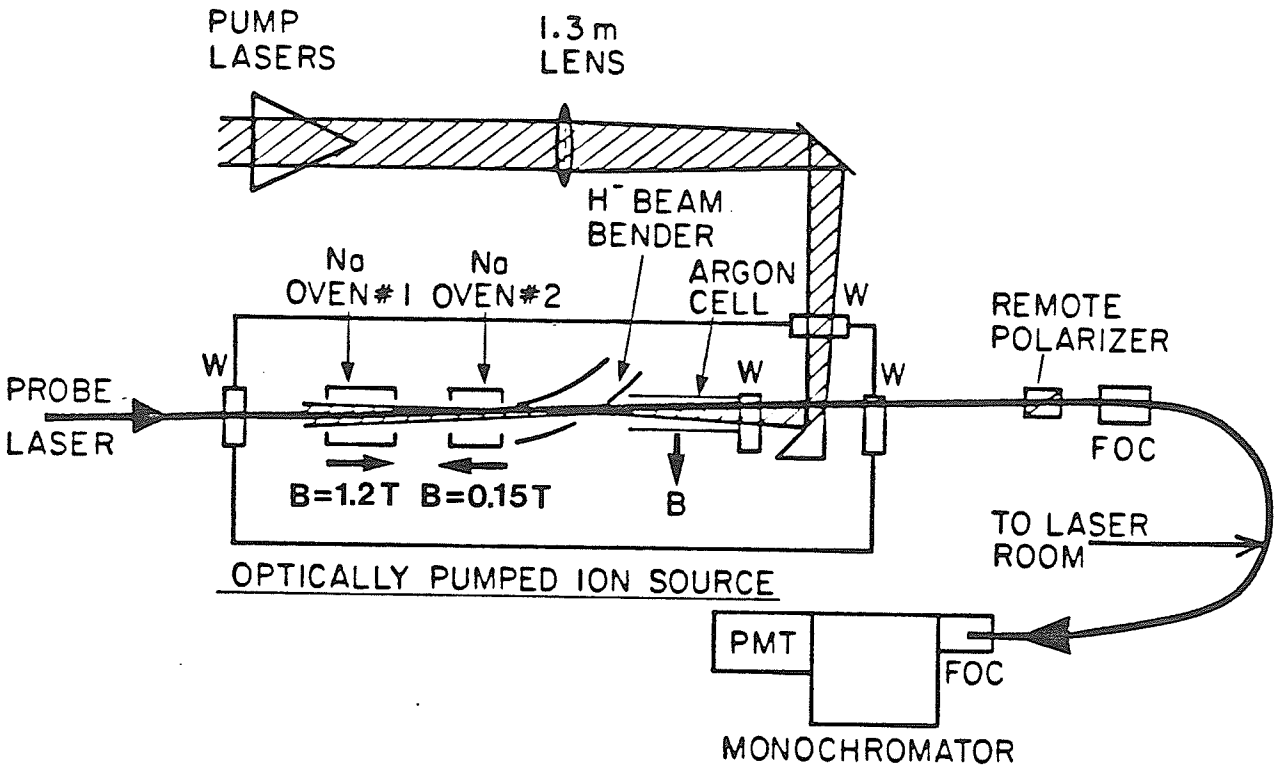

Figure 2.3: A schematic showing the pumping and probe laser beams entering the TRIUMF OPPIS.

charge exchange of the incident H^0 neutrals with the argon gas to avoid the neutrals damaging the laser window that protects the prism. A transverse magnetic field is applied to this gas cell to eliminate any charged particles produced by charge exchange of H^0 neutrals with the argon gas in the cell.

2.4 Polarization transfer efficiency

A critical step in OPPIS is the transfer of polarization from the Na to the H^0 neutrals emerging from the neutralizer. A parameter T_p, defined as the ratio of electron polarization of the H^0 beam to Na polarization, has been measured to check the feasibility of OPPIS as it determines an upper limit to nuclear polarization of the beam.

It is, in general, difficult to measure the vector polarization of protons having energy below several hundred keV. Instead, the tensor polarization of a deuterium beam was measured, assuming that T_p is the same for both protons and deuterons as the transfer is purely atomic. The asymmetric angular distribution of neutrons at 0° and 90° from the reaction $^3H(\vec{d},n)^4He$ was used to measure the tensor polarization of the D^- beam. To increase the neutron production rate, the D^- beam was accelerated an additional 50 keV above the original beam energy (5 keV) by applying a +50 kV bias on the titanium tritide target. It was found that $T_p = 0.62 \pm 0.09$ at a magnetic field of 1.26 T for a deuteron beam at 5.0 keV [13], whereas calculations predict $0.8 \leq T_p \leq 0.85$ [14]. The discrepancy between the experimental and calculated values was mainly due to the neutral D^0 beam contamination in the D^+ beam originating in front of the entrance to the Na neutralizing cell. The neutral beam contamination was mostly created by collisions between the D^+ beam and the residual D_2 gas molecules between the ECR source and the Na neutralizing cell.

Theoretical calculations [14] also suggest that the transfer efficiency increases with higher magnetic field in the Na neutralizer region. It is planned to replace

the conventional solenoids in the neutralizer region with superconducting coils, thus increasing the magnetic field to 2.0-2.5 T, where the polarization transfer efficiency should be at least 85%.

2.5 Ionizer

The neutral H^0 beam emerging from the neutralizer enters a second alkali cell (ionizer), where the H^0 neutrals are ionized by charge exchange, $H^0 + Na \longrightarrow H^- + Na^+$, to form nuclearly polarized H^- ions. Sodium is also used as an electron donor in the ionizer because of its relatively high H^- equilibrium yield [12]. The oven of the ionizer is usually maintained at ~300°C and the corresponding thickness of Na vapour is $\sim 10^{15}$ atoms cm^{-2}. A pair of air-cooled baffles kept at ~150°C is used to confine the vapour. The outlet aperture of these baffles is 7 mm so that an H^- beam with suitable emittance is selected, and the effective length of the cell is about 65 mm. The ionizer is embedded in a 0.16 T magnetic field to preserve the nuclear polarization of the H^- beam during charge exchange. The emittance of the H^- beam has been measured as a function of the ionizer magnetic field.

From the H^- beam emittance measurements, two different emittances are observed. In addition to the 5 keV H^- beam, there is also a small 2.5 keV H^- component resulting from the 5 keV H_2^+ produced by the ECR source. The ionizer is therefore biased at several hundred volts so that particles experiencing charge exchange in the neutralizer and ionizer can be distinguished by their energies.

2.6 Transport beamline to the accelerating column

A short beamline has been designed and assembled inside a large vacuum chamber to transport the H^- beam emerging from the ionizer to the 300 kV accelerating column. This beamline consists of a pair of electrostatic bends, a pair of einzel lenses, a Wien filter and some beam steering elements (fig. 2.1).

2.7 Vacuum system

The vacuum of the TRIUMF OPPIS is maintained by 3 cryopumps (each 1500 Torr l/s H_2), one of which is under the chamber containing the pair of deflectors, and the other two are under the large chamber containing the transport beamline. The pressures in these two chambers are about 3×10^{-6} Torr during the operation of the source. The source is occasionally vented in order to clean the electrodes and to load Na metal into the cells, and can be pumped down from atmospheric pressure to $\sim10^{-6}$ Torr in an hour. A gate valve between the vacuum chamber containing the pair of deflectors and the ionizer solenoid allows source maintenance without affecting the transport beamline pressure. Figure 2.4 is a schematic diagram showing the vacuum system in the TRIUMF OPPIS.

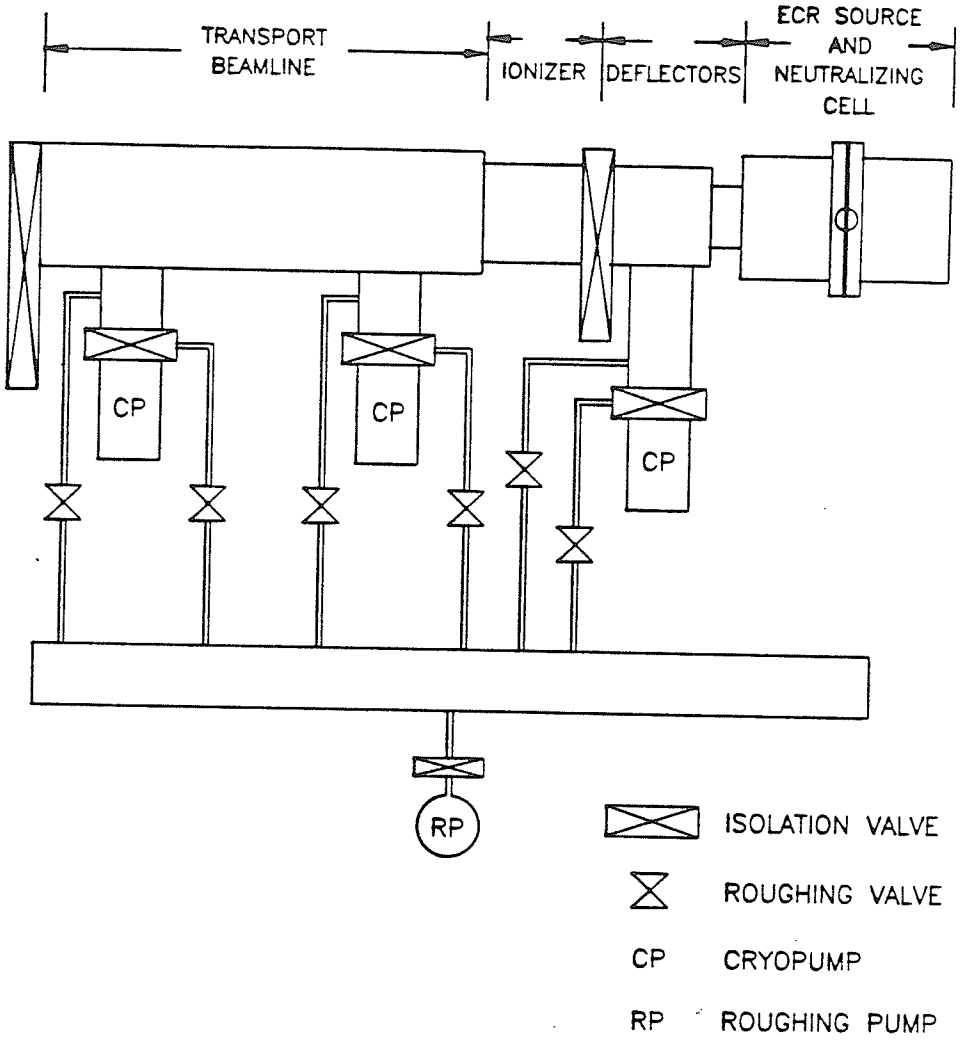

Figure 2.4: A schematic diagram showing the vacuum system in the TRIUMF OPPIS installed on the HV terminal.

Chapter 3

Wall Relaxation Measurements

3.1 Overview

In OPPIS, it is neccessary to produce high atomic polarization of sodium vapour by laser optical pumping. Wall surfaces with low polarization relaxation rates are important in the polarized Na vapour charge exchange target used in OPPIS. Swenson and Anderson [16] have measured wall relaxation rates for a variety of wall surfaces at typical operating temperatures of 200-300°C . The most useful material, a mixture of methyltrimethoxysilane and dimethyldimethoxysilane, baked onto a copper substrate ("dry-film"), allowed up to 1000 (e^{-1} relaxation) wall collisions per sodium atom before depolarization occurred. They also observed the depolarization of sodium atoms after one collision with metal surfaces, namely, stainless steel, anodized aluminum and chrome plated copper surfaces. Their results were obtained by observing the relaxation of the hyperfine level population difference $\langle \mathbf{S} \cdot \mathbf{I} \rangle$ at low magnetic fields (1-20 G), and it was assumed that the high field relaxation of the electron spin longitudinal polarization $\langle S_z \rangle$ was the same, based on the theoretical and experimental work of Bouchiat and Brossel on rubidium atoms [17].

In this chapter, direct measurements made of $\langle S_z \rangle$ wall relaxation of optically pumped sodium atoms at high magnetic fields are reported, using dry-film coatings,

uncoated 316 stainless steel and copper walls. As expected, a dry-film coated wall is effective in preventing depolarization at high fields. A copper wall has been found to be less depolarizing at high magnetic fields. Although Zelenskii et al. [18] first reported the persistence of sodium vapour polarization in stainless steel charge exchange targets in fields of 10-20 kG, no significant changes in depolarization rates with applied magnetic field using stainless steel walls has been observed.

3.2 Preparation for different wall surfaces

The copper and stainless steel target cells were prepared by machining either ordinary copper or 316 stainless steel into cylindrical tubes, and then cleaned thoroughly with acetone. The dry-film coated cell was prepared by first cleaning a copper liner very well with boiling distilled water and then with methanol. A mixture of 80% distilled water, 10% dimethyldimethoxysilane and 10% methytrimethoxyacetic acid was prepared. The copper liner to be coated was then left in the mixture for 2 or 3 days until a layer of gel had formed on the bottom of the glass container. After the gel appeared, the coating was ready. The copper liner was removed from the mixture, and was baked at about 200°C for approximately 3 hours in a vacuum chamber. After baking, the coated part appeared shiny. The coating was tested by squirting a few drops of distilled water on it. The water beaded up and ran off without wetting the surface.

3.3 Polarization relaxation measurement

The sodium $\langle S_z \rangle$ polarization relaxation was measured in the dark using a Faraday rotation method. When a linearly polarized light passes through a magnetized medium, the plane of polarization of the light is rotated about the optical axis, and this is called the Faraday rotation effect. An unstabilized Coherent-699 ring laser (bandwidth 2 GHz) provided a beam of linearly polarized light at 589.3 nm,

midway between the two sodium D lines, and served to probe the sodium vapour. A 6 GHz bandwidth Coherent 590-03 broadband laser (modified by a 0.5 mm thick intra-cavity etalon) optically pumped the sodium vapour with circularly polarized light at 589.6 nm. Figure 3.1 shows schematically the experimental arrangement. The power of the 2 mm diameter probe beam was < 1 mW. The pump beam (0.6 W) was adjusted to fill the 4.8-4.9 mm inner diameter cylindrical target cell. The 66 mm long sodium cell was situated within a uniform longitudinal magnetic field which was varied between 0.05 and 1.2 T. Sodium atoms entered the optical pumping region through a 2 mm diameter aperture from a liquid sodium reservoir below. The sodium density outside the cell was kept very low by cooled 8 mm diameter aperture condensers at both ends of the cell. The sodium target was contained in a vacuum chamber maintained at $< 10^{-6}$ torr by turbo- and cryopumps. Fused silica windows at both ends of the chamber transmitted the laser beams.

The thickness nl of the sodium vapor was found from the Faraday rotation of the linear polarization of the probe beam, θ_0, produced when the magnetic field was on. The steady state $\langle S_z \rangle$ polarization P_0 of sodium atoms achieved by optical pumping was found from the further Faraday rotation, θ_p, of the linear polarization of the probe beam, which occured when the pump beam was on. The thickness nl in atoms cm^{-2} and P_0 are given, in terms of the Faraday rotation angles in degrees and the magnetic field strength B in T, as [19]

$$nl = \frac{1.61\theta_0}{B} \times 10^{13} \tag{3.1}$$

and

$$P_0 = \frac{\theta_p}{\theta_0} \frac{B}{10.12} \tag{3.2}$$

where θ_0 and θ_p are within typical rotations of $\sim$3-4° and $\sim$10° at $B = 1.2$ T, respectively; nl is within 4-5$\times 10^{13}$ atoms cm^{-2}.

Rotation angles were measured by rotating polarizer ♯2 (see fig. 3.1) so as to produce minimum transmission of the probe beam, and then equating the amount of rotation necessary to produce a new minimum transmission of the probe beam

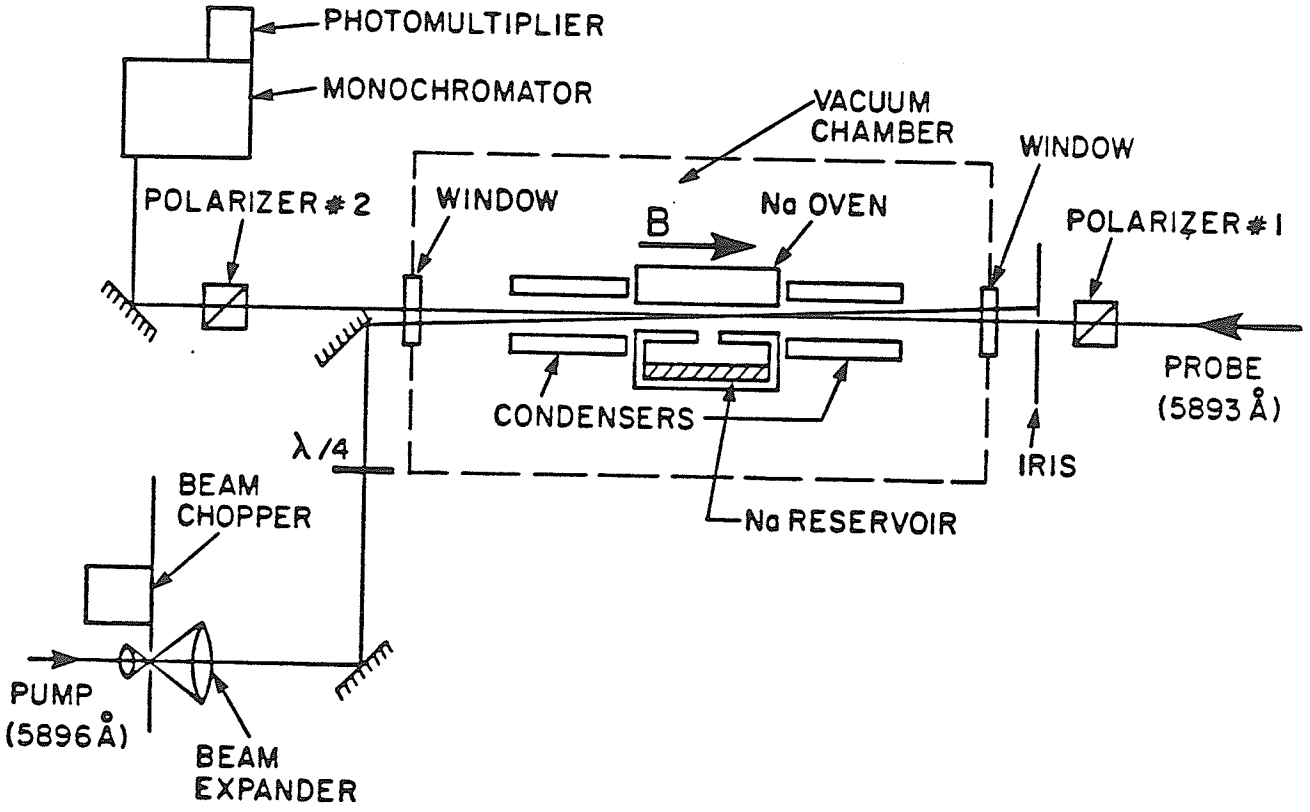

Figure 3.1: Experimental arrangement for the wall relaxation measurements.

to any change in Faraday rotation within the sodium vapour. The correctness of this procedure was checked by rotating polarizer ♯1 a known amount and confirming that the same rotation was necessary in polarizer ♯2 to produce a new minimum. The accuracy in measuring the rotation angles was within a tenth of a degree.

After calibrating the system with a steady state polarization measurement (as described above) for a given set of experimental conditions, polarizer ♯2 was re-set to produce minimum transmission of the probe beam for zero sodium polarization. The pump beam was then chopped at 120 Hz with a pulse width of 230 μs, which allowed the $\langle S_z \rangle$ polarization of sodium atoms to reach the steady state value. Figure 3.2 shows the photomultiplier signal when the pump beam was on and off. A Tektronix 2430 digital oscilloscope was used to signal average and store the photomultiplier output. The signals were transformed into time dependent polarization $P(t)$ according to (see Appendix A for derivation)

$$P(t) = \frac{P_0}{\theta_p} sin^{-1} \left[\frac{S(t)}{S(0)} sin^2(\theta_p) \right]^{1/2} \tag{3.3}$$

where $S(t)$ is the photomultiplier signal as a function of time and $S(0)$ is the signal at the instant when the pump laser beam is chopped off. The chopper system time resolution of 1.5 μs, obtained from the decay time constant of the chopper signal (fig. 3.2), corresponded to a resolution of 3 μs when transformed into $P(t)$. Figure 3.3 plots examples of the raw relaxation signals from the oscilloscope traces and their transformed polarization relaxation from eq.(3.3) in semi-logarithmic co-ordinates for dry-film, copper wall and stainless steel target cells. The exponential decay curve was fit to a single relaxation time T_{obs}. The polarization relaxation was measured as a function of the magnetic field within the range 0.05 - 1.2 T. A fast decay rate, limited by the time resolution of the detecting system, was not included in the fit for T_{obs}. At magnetic fields less than 0.2 T, the relaxation time T_{obs} of the $\langle S_z \rangle$ polarization, determined from the slope of the exponential decay curve (fig. 3.3), is unaffected by the precise value assigned to the steady state polarization, which was

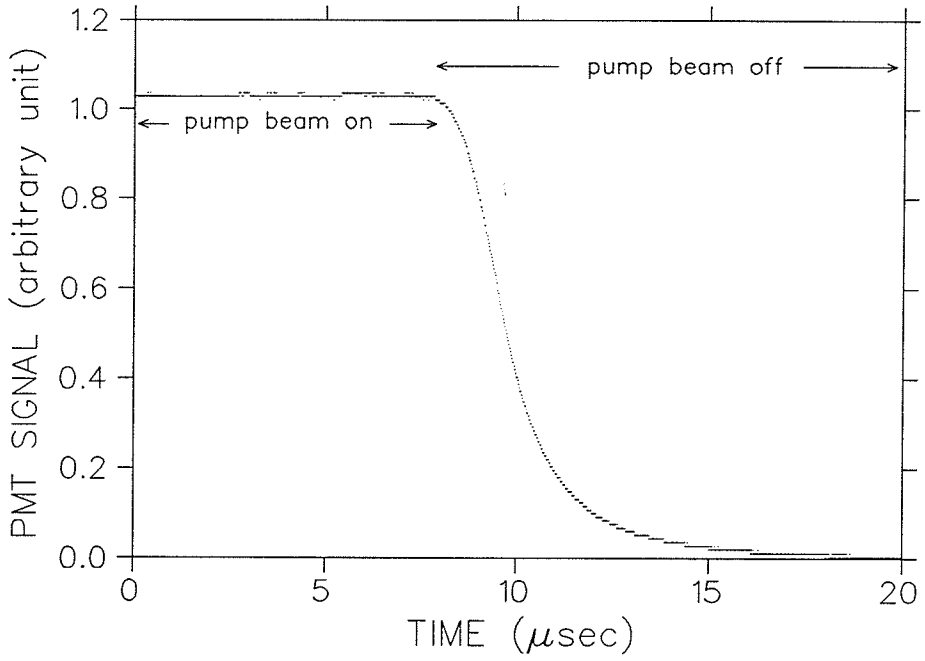

Figure 3.2: Photomultiplier (PMT) signal when the pump beam was on and off.

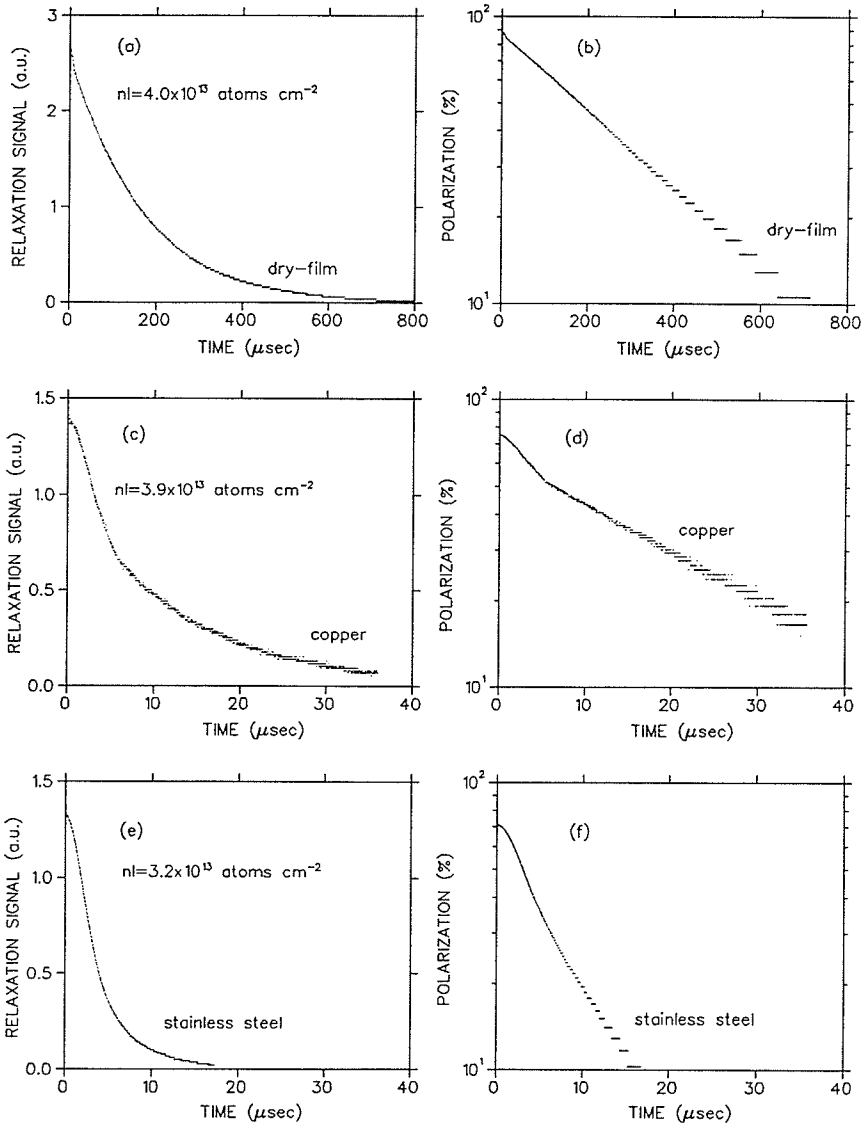

Figure 3.3: Raw relaxation signals from the oscilloscope traces and their transformed polarization relaxation of Na atoms in different target cells. The applied magnetic field was 1.2 T. (a) and (b) dry-film coated wall, inner diameter = 4.8 mm; (c) and (d) copper cell, inner diameter = 4.9 mm; (e) and (f) stainless steel cell, inner diameter = 4.85 mm.

not accurately determined by the Faraday rotation method at such low magnetic fields.

3.4 Relaxation results and analysis

The experimentally observed $\langle S_z \rangle$ polarization relaxation time T_{obs} is given by the expression

$$T_{obs}^{-1} = T_m^{-1} + T_w^{-1} \tag{3.4}$$

where T_w is the relaxation time due to wall collisions and T_m is that due to molecular flow of the atoms out of the cell through the exit apertures and reservoir entrance. In fig. 3.4, T_{obs} is plotted as a function of the applied magnetic field for different wall surfaces. The sodium thickness was $\sim 4 \times 10^{13}$ atoms cm^{-2} and at this thickness, the steady state polarization of Na vapour achieved by laser optical pumping is not limited by radiation trapping [20]. In other experiments, no significant correlation was found between the sodium thickness and T_{obs} over thicknesses 2.6-11.1$\times 10^{13}$ atoms cm^{-2}, implying that the relaxation time T_{obs} of the $\langle S_z \rangle$ observable is effectively independent of spin exchange collisions between sodium atoms at these thicknesses.

The purpose of the present work was to determine T_w for the cells with copper or stainless steel walls, and hence the mean number of non-depolarizing wall collisions $N = T_w D/\overline{v}$, where D is the target cell inner diameter and $\overline{v}$ is the mean thermal velocity of sodium atoms at a temperature of 240°C corresponding to sodium thickness of $\sim 5 \times 10^{13}$ atoms cm^{-2}. To determine T_w from eq.(3.4) and hence N, one also needs to know T_m, which depends on the cell geometry and was assumed to be independent of the wall material. As reported by Swenson and Anderson [16] for their cell geometry, the observed relaxation time for dry-film coated wall was nearly equal to the relaxation time T_m. For the cell geometries used in the present work, T_m was calculated to be ~ 250 μs using the pumping conductance [21] for the atoms flowing out of the cell through the exit apertures and reservoir entrance, and was compara-

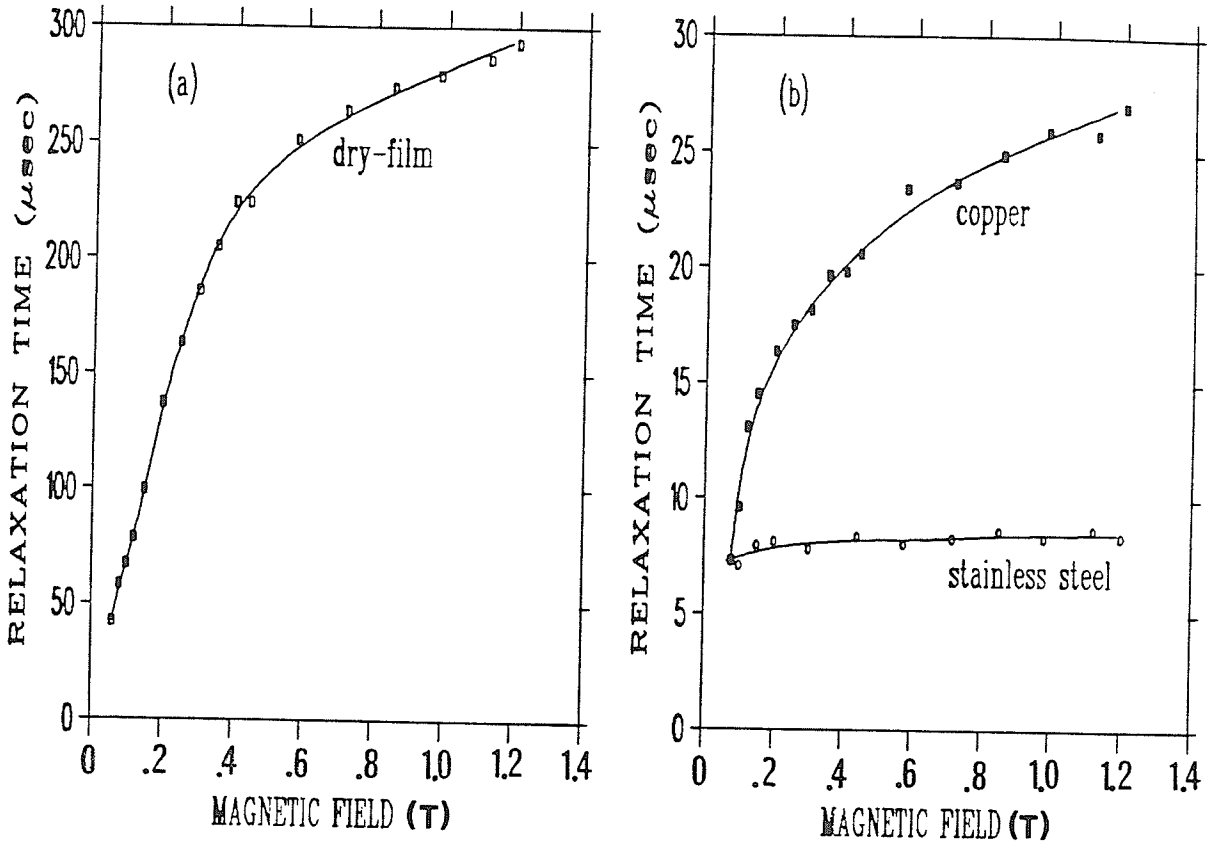

Figure 3.4: Observed relaxation time T_{obs} as a function of applied magnetic field; (a) dry-film coated wall, (b) copper wall and stainless steel wall. A small correction to T_{obs} has been made accounting for the time resolution of the detecting system. The curves are smooth curves to the data points.

ble to the observed relaxation time (~300 μs) for dry-film coating data at high field (fig. 3.4(a)). Hence T_m was estimated to be 300 μs using the dry-film coating data at high field. Figure 3.5 shows the variation of N as a function of magnetic field for a copper wall. It can be seen that at high fields, N increases to 4. However from fig. 3.4(b) the wall relaxation time for the stainless steel wall remained very close to the time for one wall collision (7 μs) even at high fields. Figure 3.4(a) shows that the effectiveness of the dry-film coating in preventing depolarization also increases with applied magnetic field. A similar effect with paraffin wall coatings and polarized rubidium atoms has been previously reported [17].

Figure 3.6 shows the magnetic field dependence of the steady state $\langle S_z \rangle$ polarization of sodium atoms for the different wall materials, showing progressive improvement going from stainless steel to copper to dry-film coated walls. Such improvement is due to the different relaxation times associated with the wall materials. The equilibrium value for the sodium polarization increases as the rate of depolarization is decreased while maintaining the polarization rate due to optical pumping. Therefore higher steady state polarization can be achieved with the surfaces having a longer relaxation time.

3.5 Calculation of local magnetic field and correlation time

Upon striking the wall of the target cell, an atom does not necessarily immediately rebound, but can be adsorbed by the surface for a finite time before it returns back into the cell. During this time, the atom is subjected to a local magnetic field induced by the vibrational motion of the atoms of the wall, and consequently the orientation of its atomic magnetic moment with respect to the external magnetic field can be destroyed. As pointed out by Bouchiat and Brossel in the case of rubidium atoms [17], the effect of the interaction of the adsorbed sodium atom magnetic moment with

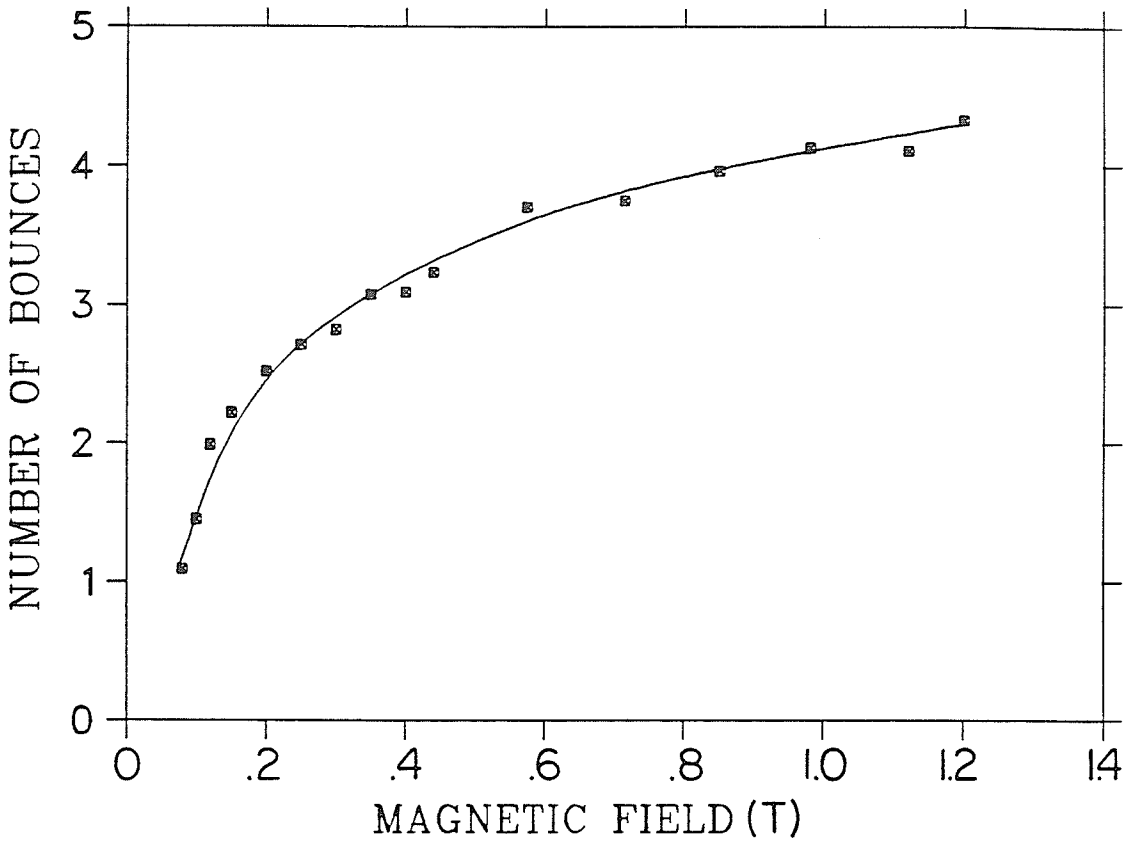

Figure 3.5: Variation of mean number of non-depolarizing wall collisions N as a function of applied magnetic field for a copper wall. The curve is a smooth curve to the data points.

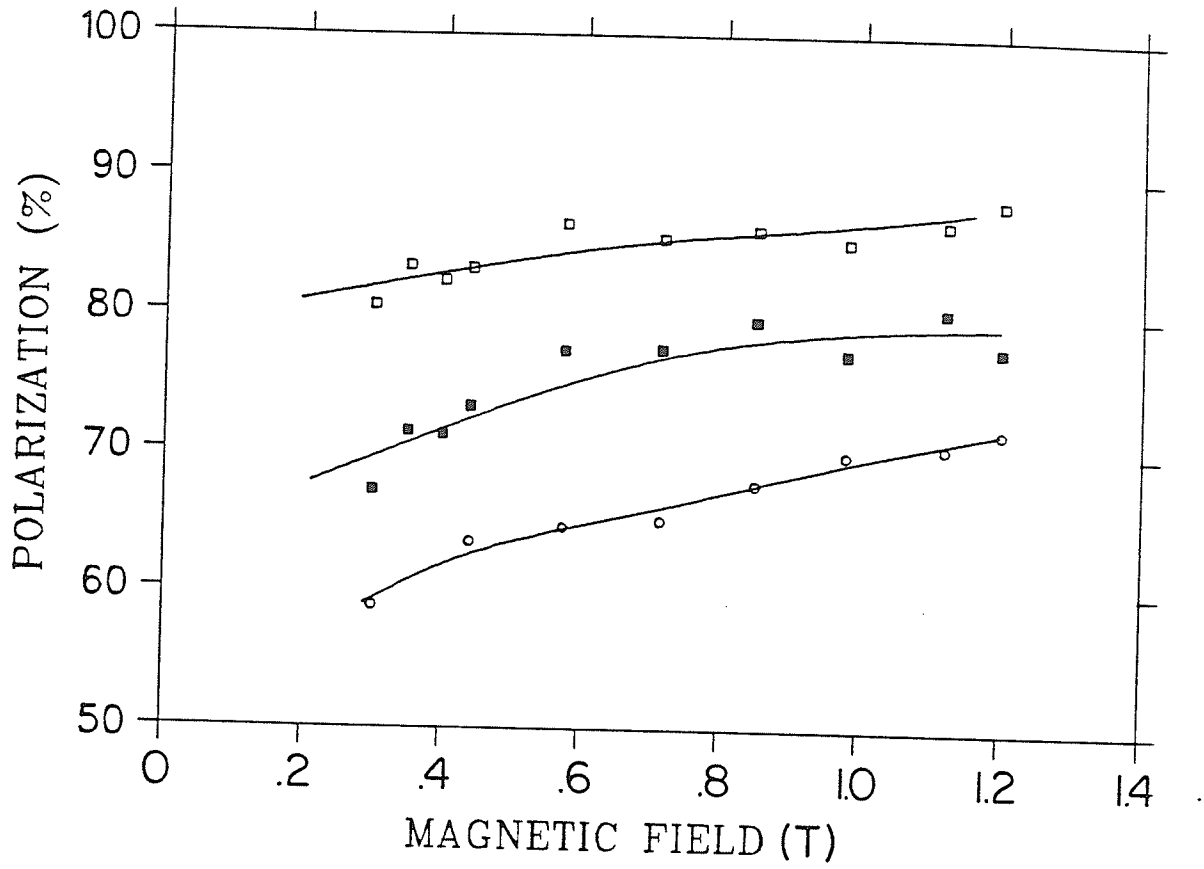

Figure 3.6: Applied magnetic field dependence of steady state Na polarization. Laser power = 0.6 W. Open squares: dry-film coating, Na thickness = 3.8×10^{13} atoms cm^{-2}; solid squares: copper wall, Na thickness = 3.2×10^{13} atoms cm^{-2}; open circles: stainless steel, Na thickness = 3.2×10^{13} atoms cm^{-2}.

the local magnetic field is to induce transitions among different (sodium) Zeeman sublevels, hence causing relaxation. It is possible from the experimental data to estimate the strength of the local field and the time the atoms dwell on the wall before returning back into the cell. The strength of the local field can explain the observed difference in the $\langle S_z \rangle$ wall relaxation times of sodium atoms on copper, stainless steel and dry-film coated walls.

The observed wall relaxation rate T_w^{-1} as a function of the external magnetic field B shows that T_w^{-1} has two components, one of which is B dependent ($T_{s1}^{-1}(B)$) and the other is B independent at high fields (T_{s2}^{-1}). T_w^{-1} can be written as the sum of the two components, i.e.

$$T_w^{-1} = T_{s1}^{-1}(B) + T_{s2}^{-1}. \tag{3.5}$$

The field dependent wall relaxation rate $T_{s1}^{-1}(B)$ of an isolated spin **S** in an external magnetic field is given by [17]

$$T_{s1}^{-1}(B) = Cj(\omega) \tag{3.6}$$

where

$$j(\omega) = (1 + \omega^2 \tau_c^2)^{-1} \tag{3.7}$$

is the spectral density function with correlation time τ_c and ω is the Larmor frequency for the electron spin in the external magnetic field. The coefficient C, interpreted as the amplitude of the relaxation rate, is given by

$$C = \frac{2}{3} \frac{\tau_s}{\tau_s + \tau_f} \gamma^2 h^2 \tau_c \tag{3.8}$$

where τ_s is the dwell time of an atom on the wall at each wall collision, γ is the gyromagnetic ratio of the electron, h is the local magnetic field strength at the wall, and τ_f is the flight time (7 μs for the cell geometries used) of the atom between wall collisions.

In the wall relaxation calculation, it is usual to approximate $\tau_s \approx \tau_c$ [16,17] and

since $\tau_f \gg \tau_s$, eq.(3.8) is reduced to

$$C = \frac{2}{3}\frac{\gamma^2 h^2 \tau_c^2}{\tau_f}. \tag{3.9}$$

$T_{s1}(B)$ can then be written as

$$T_{s1}(B) = \frac{1}{C}[1 + (\frac{eB}{m}\tau_c)^2] \tag{3.10}$$

where $\frac{e}{m}$ is the charge-mass ratio of an electron. Plotting $T_{s1}(B)$ against B^2 gives the values of $\frac{1}{C}$ from the vertical intercept and of $\frac{1}{C}(\frac{e}{m}\tau_c)^2$ from the slope. Using these relationships, τ_c and h were obtained from the field dependent relaxation data for different wall materials and are tabulated in Table 3.1. The error estimates were derived from the statistical errors in the data analysis and from the systematic errors associated with the measurable quantities, namely, the Faraday rotation angles and the applied magnetic field. The rotation angles could be measured to an accuracy of $\pm 0.1°$, which, in the worst case, contributed to an error of 5% at low magnetic field (0.1 T) and to an error of 2% at high field (1.2 T). The current in the applied magnetic field could be set to an accuracy of 0.1%, although the absolute field was not measured better than 2%. The errors associated with the fitted values for the non-field dependent term (T_{s2}) were ~3%, and were significant to the error derivation for h and τ_c. Other less significant sources of errors were the flight time τ_f (± 0.07 μs) of the atom between wall collisions arising from the uniformity of the inner diameter of the cells and the resolution of the exponential relaxation in the time dependent polarization (~2%).

As seen from Table 3.1, the local field for the stainless steel wall is twice as strong as that of the copper wall, implying that atoms relax faster on the stainless steel surface than on the copper surface. The dry-film coated wall has a relatively weak local field and therefore the atoms can have a large number of wall bounces before depolarization occurs.

Table 3.1: Tabulation of local magnetic field and correlation time for different wall materials.

	Local Magnetic Field h (T)	Correlation Time τ_c (10^{-12} sec)
Stainless steel wall	0.401 ± 0.032	6.6 ± 0.3
Copper wall	0.214 ± 0.013	19.4 ± 0.8
Dry-film coated wall	0.048 ± 0.004	82.5 ± 4.9

3.6 Summary of the chapter

The $\langle S_z \rangle$ wall relaxation time of optically pumped polarized sodium atoms on stainless steel, copper and dry-film coated walls has been measured as a function of the external magnetic field. It has been shown that the mean number of wall collisions on a copper wall increases to about four at high field before depolarization occurs, whereas the atom depolarizes after a single collision on a stainless steel surface. The dry-film coated wall can allow more than 40 wall collisions, and is very effective in preventing depolarization. The differences in the depolarizing properties among the materials used are a consequence of different strengths of the local magnetic field at the wall surface.

One problem of the dry-film coated wall, affecting the performance of optically pumped polarized ion sources, is the rapid destruction of the coating when the sodium vapour is used as a charge exchange target. However, sodium atoms, even in an uncoated copper cell, can be 80% polarized at a target thickness of 4×10^{13} atoms cm^{-2} (fig. 3.6) by a 0.6 W laser beam. Increasing the laser power by a factor of 2-3 should increase the steady state polarization of the sodium atoms to nearly 100%. To achieve the same polarization with a stainless steel cell requires considerably more laser power, which is relatively expensive. Therefore, copper is

believed to offer good promise as a wall surface for use on polarized charge exchange target cells in the optically pumped polarized ion sources.

Chapter 4

σ_{+0} Measurements of $H^+ \longrightarrow H^0$ in Na Vapour

4.1 Overview

The determination of the charge neutralization cross section σ_{+0} for the reaction $H^+ + Na \longrightarrow H^0 + Na^+$ has been studied both theoretically [22] and experimentally [12,23], and its value is an important parameter to determine the percentage of the incident H^+ beam being neutralized in optically pumped polarized H^- (or H^+) ion sources. In all experimental measurements of σ_{+0} so far, the Na target thickness has to be determined. Most previous measurements have relied on target temperature measurements to obtain the Na vapour thickness from vapour pressure data. In some recent reported values of σ_{+0} [23,12] the uncertainty in the measurement of target thickness was estimated to be 15-20%.

In this chapter, an experimental setup used in a previous measuremnt of σ_{+0} is briefly described. Then a new approach is reported, that uses the Faraday rotation method which does not rely on temperature measurements to determine the values of σ_{+0} (at incident H^+ ion energies of 2.6, 5.0 and 8.0 keV) and typically gives the Na thickness to an accuracy of 5%.

4.2 Previous experimental setup

The apparatus used in a previous experiment [12] is schematically shown in fig. 4.1. A beam of H^+ ions was extracted from a duoplasmatron ion source, and was then momentum analysed by a 10° bending magnet. The beam was collimated by a pair of defining apertures. Following the collimation section, the ion beam passed between two parallel electrostatic beam deflection plates which deflected the beam into a suppressed Faraday cup located off the beam axis. The measured incident current, I_s, was given by $I_s = qN_s$, where q was the electronic charge and N_s was the number of H^+ ions incident per second on the target. When the plates were grounded, the ion beam passed the plates undeflected and entered the Na target.

The Na vapour target was 165 mm long and was constructed from stainless steel. To reduce the Na vapour flow out of the target, stainless steel tubes 51 mm long and 6.4 mm inner diameter were used for the entrance and exit apertures. The Na vapour pressure as a function of the Na temperature was known [24], and the Na vapour density, n, in the target was then calculated from the Na vapour pressure and the temperature of the target [24]. The target thickness, in atoms cm^{-2}, was given by

$$\pi = n\left[L + \frac{1}{2}(L_{ent} + L_{exit})\right] \tag{4.1}$$

where L was the length of the target cell, L_{ent} and L_{exit} were the lengths of the entrance tube and exit tube respectively. The uncertainty in the measurement of the target thickness was estimated by Anderson et al. [12] to be ±20% primarily due to the uncertainty in the vapour pressure of Na as a function of the target temperature.

A magnet located after the exit aperture of the Na target cell deflected the H^+ and H^- ions emerging from the target into two suppressed Faraday cups located at 4° on each side of the beam axis. The currents measured by these Faraday cups were $I_+ = qN_+$ and $I_- = qN_-$ where N_+ and N_- were repectively the number of positive and negative ions incident per second on the positive and negative Faraday

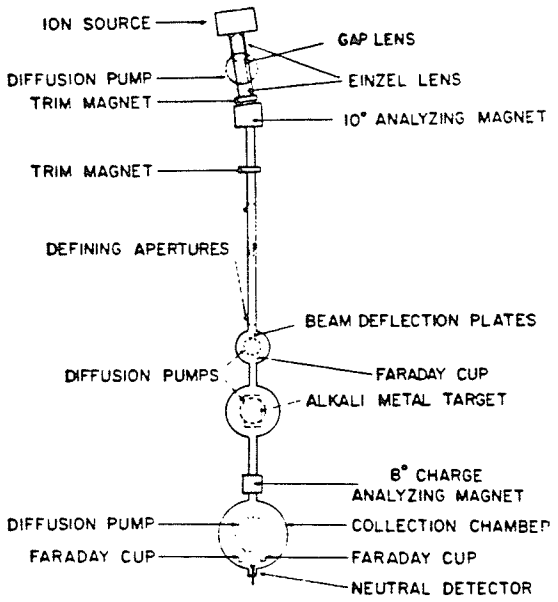

Figure 4.1: A schematic diagram showing the apparatus used by Anderson et al for the charge neutralization cross section measurements for $H^+ \longrightarrow H^0$ in Na vapour.

cups.

The neutral beam was incident on a heated and polished copper disc. The secondary electrons ejected from the disc by the incident neutrals were collected by a positively biased ring located in front of the copper disc. The current to the ring was $I_0 = qN_0R(E)$, where N_0 was the number of neutrals per second incident on the copper disc, and $R(E)$ was the average number of electrons ejected from the copper disc per incident neutral.

Therefore by measuring the currents I_s, I_+, I_- and I_0 simultaneously at different target thicknesses, Anderson et al. [12] have measured σ_{+0} for 1-25 keV H^+ ions incident on a Na vapour target.

4.3 Experimental setup for the present work

Figure 4.2 shows schematically the experimental arrangement using the Faraday rotation method to measure the Na thickness. A Na oven target cell of length 66 mm and diameter 33 mm was situated within a uniform 1.2 T longitudinal magnetic field. The Na thickness outside the cell was kept very low by cooled 8 mm diameter aperture condensers (at about 100°C) at both ends of the cell. An unstabilized Coherent-699 ring dye laser (bandwidth 2 GHz) provided a beam of linearly polarized light at a wavelength midway between the two Na D lines (i.e. 589.3 nm) and served to probe the Na vapour. The method to measure the target thickness from the Faraday rotation θ_0 of the probe beam within the Na vapour (fig. 4.2) has been described in chapter 3 (section 3.3). The target thickness nl, in atoms cm^{-2}, is given by [19]

$$nl = \frac{1.61\theta_0}{B} \times 10^{13} \tag{4.2}$$

where θ_0 is in degrees and B is the longitudinal magnetic field in T, both of which can be measured accurately, leading to the 5% error estimation.

The H^+ beam, extracted from the ECR ion source, passed through the target

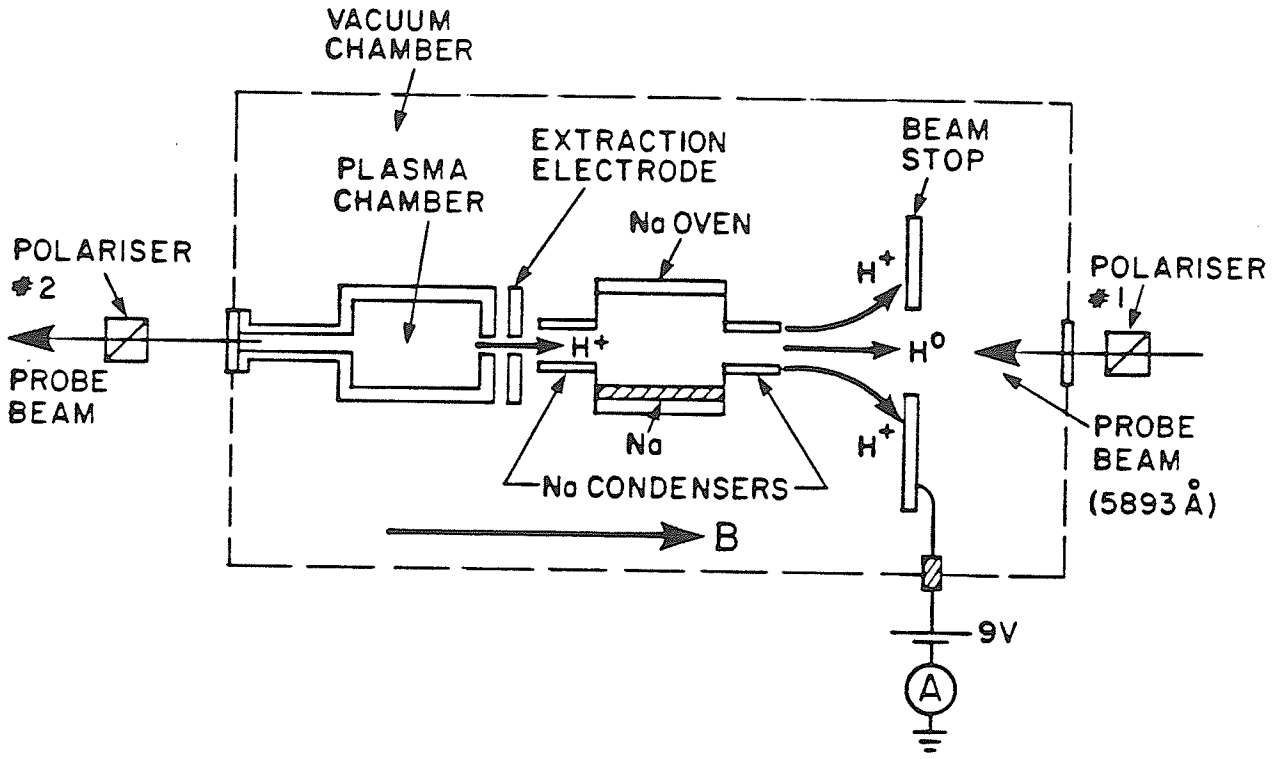

Figure 4.2: Experimental setup for the charge neutralization cross section measurements for $H^+ \longrightarrow H^0$ in sodium vapour, using the Faraday rotation method to measure the Na thickness.

cell and was intercepted by an annular beam stop situated about 200 mm from the exit of the solenoid. Both the ion source and the target cell were located inside the solenoid. The beam stop was biased +9V to recapture secondary electrons. A 10 mm diameter aperture on the beam stop, on axis with the ion beam, allowed the probe laser beam to pass through the cell and also minimized the interception by the beam stop of the neutral H^0 beam produced within the target cell. The H^+ ions leaving the cell were defocused, so that the beam stop measured a known fraction of the post-sodium-cell H^+ current. Preliminary measurements showed that the ion beam extracted from the quartz-lined ECR plasma chamber could be contaminated by up to 25% of H_2^+ and H_3^+ ions. Any errors due to the presence of these ion species were minimized by the smaller deflection of the heavy H_2^+ and H_3^+ ions relative to that of H^+ in the fringe field, and hence significantly smaller proportions of H_2^+ and H_3^+ ions were detected by the beam stop.

As the Na vapour thickness was increased from zero, the measured H^+ current, I, began to drop. I is given by

$$I = I_+ e^{-nl\sigma_{+0}} \tag{4.3}$$

where I_+ is the H^+ current at zero Na thickness. A semi-logarithmic plot of (I/I_+) against target thickness at a H^+ energy of 5.0 keV is shown in fig. 4.3. The slope of the straight line least-squares fit gives σ_{+0}. As shown, a correction to (I/I_+) was made for data at higher values of nl, compensating for the reduction in measured H^+ current due to H^- current, I_-, produced by double charge exchange in the two step process $H^+ \longrightarrow H^0 \longrightarrow H^-$ in Na. I_- was calculated according to the equation

$$I_- = (I_+ - I)\left[1 - exp(-\frac{nl\sigma_{0-}}{2})\right] \tag{4.4}$$

where σ_{0-} is the cross section for the reaction $H^0 + Na \longrightarrow H^- + Na^+$ and was taken to be (1.4-1.9)$\times 10^{-16}$ cm^2 [25] depending on the energy of the H^0 particles. In the derivation of eq.(4.4) the average position for the production of H^0 particles was assumed to be in the centre of the cell, giving a factor of 1/2 in the exponential term.

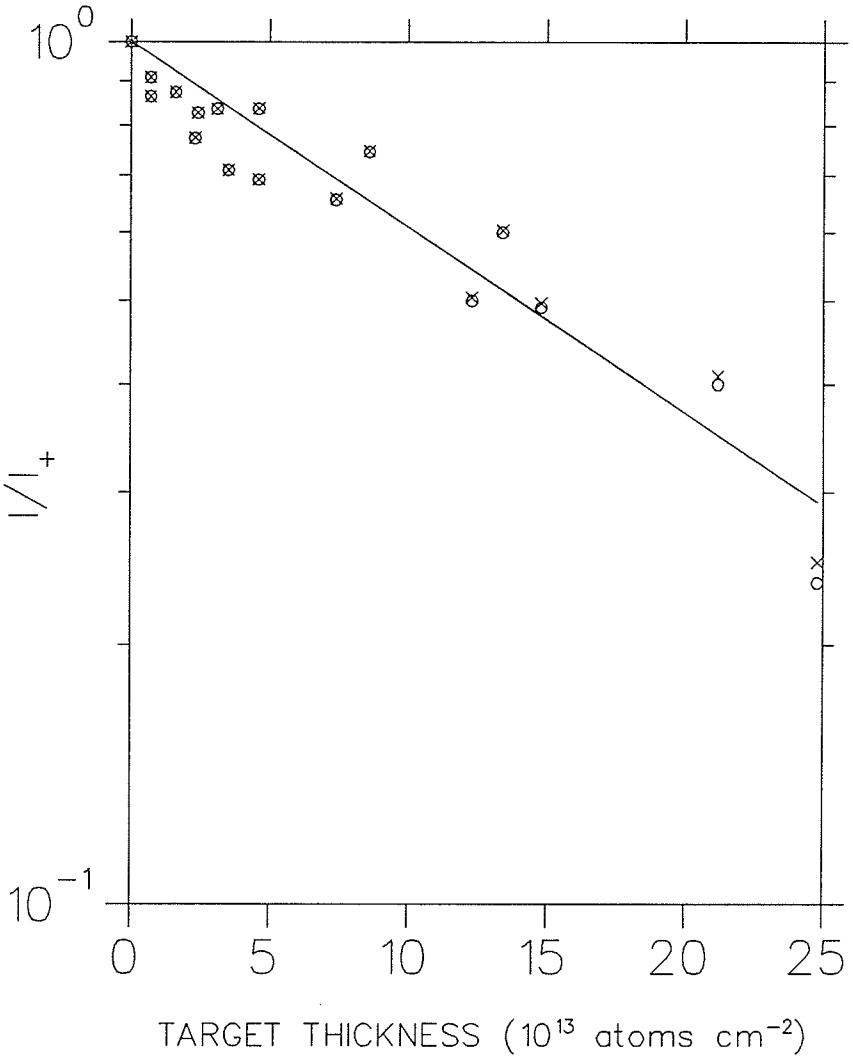

Figure 4.3: Semi-logarithmic plot of (I/I_+) against target thickness nl for a 5 keV H^+ beam. circle: data before the correction for H^- current. cross: data after correction for H^- current. The straight line was fitted for data up to the target thickness of 25×10^{13} atoms cm^{-2} after the correction for H^- current.

Table 4.1: Tabulation of charge neutralization cross section σ_{+0} for H^+ ions in Na vapour at different energies.

H^+ Energy (keV)	σ_{+0} (10^{-15} cm^2)			
	Present Work	Kimura et al. ref. [22]	Ebel & Salzborn ref. [23]	Anderson et al. ref. [12]
2.6	4.5 ± 0.5	4.7	6.7 ± 1.3*	6.6 ± 1.6*
5.0	4.9 ± 0.5	3.8	5.7 ± 1.1	6.1 ± 1.5
8.0	3.5 ± 0.6	2.5		3.7 ± 0.9

⋆ Measured at incident H^+ ion energy 2.5 keV.

Furthermore, the maximum target thickness taken in the measurement was less than 25×10^{13} atoms cm^{-2}, so that the result for σ_{+0} would be relatively independent of σ_{0-}.

4.4 Results

The results of σ_{+0} measured at different H^+ beam energies are summarized in Table 4.1, and are in fair agreement with the recent theoretical calculations of Kimura et al. [22] up to 5 keV H^+ beam energy but are at the lower range of previous experimental measurements by Ebel and Salzborn [23] and Anderson et al. [12]. The error estimates were derived from the statistical errors in the data analysis and the systematic errors associated with the Faraday rotation angles and the longitudinal magnetic field. The rotation angles could be measured to an accuracy of ±0.1°, which contributed to an error of 2% at 1.2 T magnetic field. The current in the magnetic field could be set to an accuracy of 0.1%, although the absolute field was not measured better than 2%.

As a result, the charge neutralization cross section σ_{+0} of H^+ ions in Na vapour has been measured by using the Faraday rotation method as a new approach to improve the estimate of the target thickness, hence reducing the error in σ_{+0} arising from the uncertainty in the target thickness.

Although the values of σ_{+0} are in fair agreement with recent calculations and measurements, some unavoidable systematic errors existed in these measurements. The simple beam attenuation technique used could not measure the H^- current produced in the two step charge exchange process $H^+ \longrightarrow H^0 \longrightarrow H^-$. There were H_2^+ and H_3^+ contaminants in the proton beam during charge exchange neutralization process, as the proton beam had not been subjected to momentum analysis.

To overcome these systematic errors, an analysing magnet should be used to select the H^+ ions prior to charge neutralization, and particle identification detectors should be used to measure the number of particles of H^+, H^0 and H^- simultaneously after the charge neutralization, as shown in fig. 4.4. A proton source is used to produce a beam of intense H^+ ions. A pair of defining slits allows a collimated ion beam to enter the analying magnet, with which a beam of H^+ ions is selected and its beam current is measured with a retractable Faraday cup prior to charge neutralization. Two retractable mirrors are placed upstream and downstream of the Na neutralizing cell located inside a solenoid, so that the probe laser beam can go through the cell and monitor the thickness of the target using the Faraday rotation method. A pair of electrostatic deflectors separates the H^0, H^- and H^+ components exiting the neutralizing cell, and these components are then detected simultaneously.

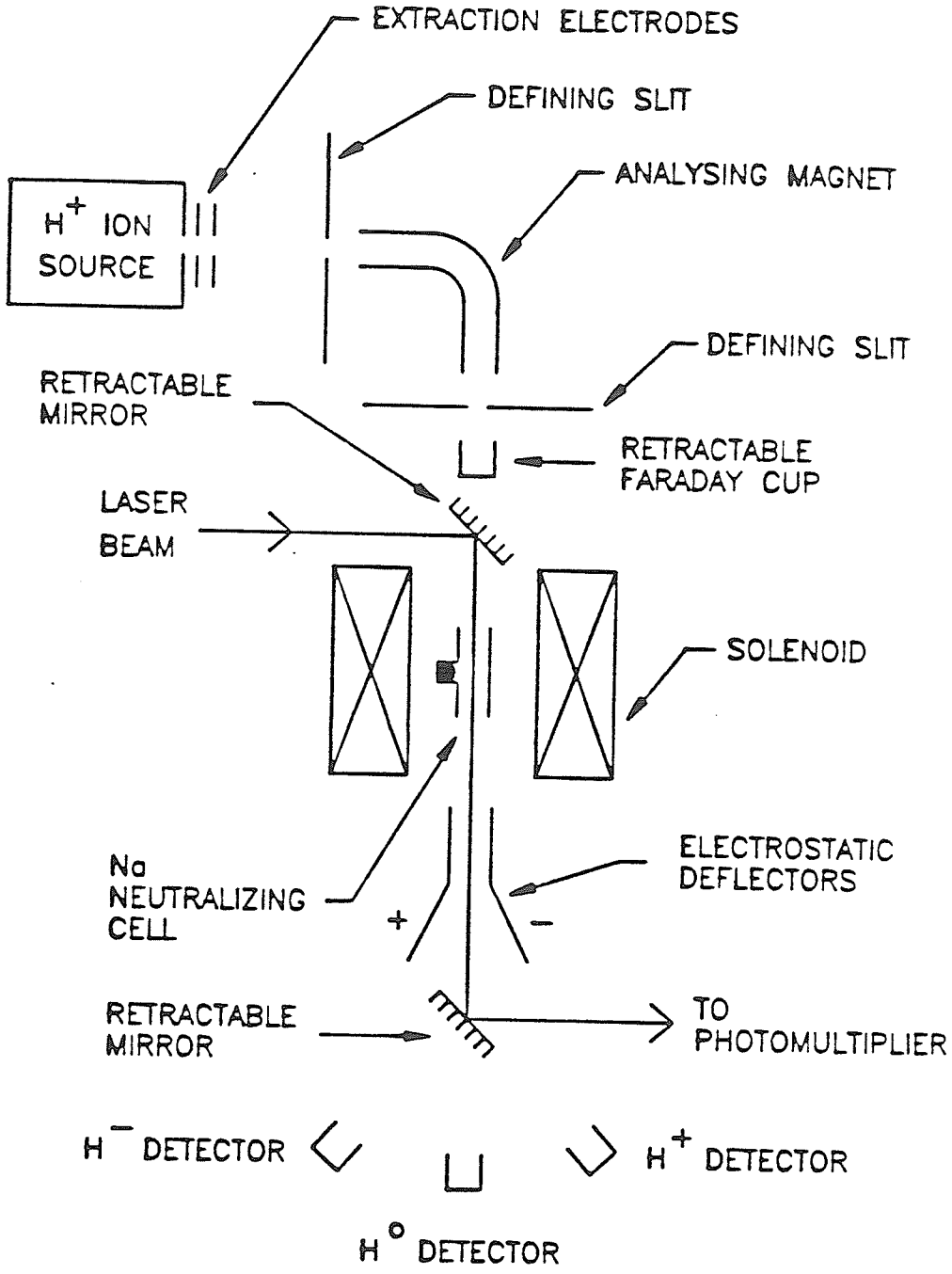

Figure 4.4: A schematic diagram of the proposed σ_{+0} experimental arrangement using an analysing magnet and particle identification detectors.

Chapter 5

Emittance and Brightness Measurements For ECR Ion Source Extraction

5.1 Overview

ECR ion sources are used as charged particle sources for accelerator injection and fundamental atomic physics research [26] as well as in the production of polarized ions [27]. Since the ECR source and its extraction system are located inside a solenoid producing an axial magnetic field, the extracted beam envelope is normally amplitude modulated with axial distance. This kind of beam dynamics is known as immersed flow. In discussing the quality of an extracted ion beam from an ECR source, the determination of the emittance parameters of the beam is important for the design and performance of the source and in particular for the beam optics problems associated with charge exchange in solenoids [28]. There are several conventional methods of measuring the beam emittance, e.g. using a movable Faraday cup or pepper-pot method [29]. However, in all these methods the measurements are carried out where the beam drifts in a field free region. These conventional methods are not suitable for the emittance measurement of the beam extracted from an ECR source, as the extraction takes place inside a solenoidal magnetic field. To obtain the beam emittance parameters at the extractor, one has to carry out the measurement

inside the solenoid in order to avoid effective emittance growth in the transverse plane due to the defocusing action of the fringing field of the solenoid [6] (also see section 6.2).

In this chapter, the design and application of a simple method are described for measuring the beam emittance parameters and then calculating the emittance and brightness of the ion beam. The quality of the extracted ion beam and the characteristics of the ion source can be interpreted from data obtained with this method. This method is generally applicable to an azimuthally symmetric ion beam extracted from an ion source with immersed flow beam dynamics.

The idea behind this method is to relate the modulated beam envelope downstream of the extractor with the three emittance parameters of the beam at the extractor, namely the beam size, angular divergence and correlation parameter, by the linear TRANSPORT formalism approach. By measuring the beam envelope radius as a function of axial distance, these emittance parameters, and hence the emittance of the beam at the extractor, can be determined.

In the following sections, the mathematical framework of the method is explained, followed by the description of the measuring device. The method has been applied to the ECR ion source employed in the TRIUMF OPPIS in order to investigate the variation of the extracted H^+ beam emittance and brightness as a function of the aspect ratio of the extraction electrodes. The results obtained are discussed in terms of the beam optics associated with the extraction system.

5.2 The beam matrix in TRANSPORT

The linear TRANSPORT formalism approach [30] has been used to relate the envelope of the modulated beam downstream of the extractor with the emittance parameters at the extractor. For a brief introduction, TRANSPORT assumes that a bundle of particle rays forming a particle beam may be represented in coordinate

phase space by a 6-dimensional ellipsoid with coordinates $(x, x', y, y', z, \delta)$. The coordinates x and y are the transverse directions, and x' and y' represent the slopes of the projection of the trajectory in the x and y direction, respectively. The quantity z represents the longitudinal direction of the particle relative to a particle travelling on the reference trajectory with the reference momentum. The last coordinate δ is the momentum difference of the particle from the reference momentum. The linear TRANSPORT approach is a matrix calculation which truncates the problem to first order in a Taylor series expansion about the reference trajectory. Particles in the beam are assumed to lie within the boundaries of the ellipsoid with each point within the ellipsoid representing a possible ray. The volume of the ellipsoid is known as the phase space volume occupied by the beam. Furthermore, the projection of the ellipsoid in any two dimensions, i.e. (x, x') or (y, y'), is a phase ellipse. The area of the phase ellipse is the beam emittance. All the important physical parameters of the beam ellipsoid may be expressed as functions of the matrix elements of the beam matrix $\sigma(z)$ at a longitudinal position z. In particular the square roots of the diagonal elements, $(\sigma_{ii})^{1/2}$, are the projections of the ellipsoid upon the coordinate axes and thus represent the maximum extent of the beam in the various coordinate directions. The correlation between components (the orientation of the ellipse) is determined by the off-diagonal terms, σ_{ij} with $i \neq j$, of the beam matrix.

5.3 Beam transport in a solenoidal field

When the beam is extracted from the ECR ion source with an energy given by the extracting potential, its initial beam matrix at the extractor is defined as $\sigma(0)$. After undergoing a matrix transformation R, the output beam matrix of the beam is

$$\sigma(z) = R\sigma(0)R^T \tag{5.1}$$

where $\sigma(z)$ is the beam matrix at a distance z downstream of the extractor and R^T is the transpose of R. Since the beam is traversing the solenoidal magnetic field,

the transformation R is the solenoidal transfer matrix given by [31]

$$R = \begin{pmatrix} 1 & \rho sin\frac{z}{\rho} & 0 & \rho(1-cos\frac{z}{\rho}) \\ 0 & cos\frac{z}{\rho} & 0 & sin\frac{z}{\rho} \\ 0 & -\rho(1-cos\frac{z}{\rho}) & 1 & \rho sin\frac{z}{\rho} \\ 0 & -sin\frac{z}{\rho} & 0 & cos\frac{z}{\rho} \end{pmatrix} \tag{5.2}$$

where $\rho = mv_z/(qB), q/m$ is the charge-mass ratio of the ion, B is the axial magnetic field strength and v_z is the axial velocity of the ion beam.

In general, the aperture of the extractor is circular and produces an azimuthally symmetric beam, so that the initial beam matrix $\sigma(0)$ at the extractor can be written as

$$\sigma(0) = \begin{pmatrix} \sigma_{11}(0) & \sigma_{12}(0) & 0 & 0 \\ \sigma_{12}(0) & \sigma_{22}(0) & 0 & 0 \\ 0 & 0 & \sigma_{11}(0) & \sigma_{12}(0) \\ 0 & 0 & \sigma_{12}(0) & \sigma_{22}(0) \end{pmatrix} \tag{5.3}$$

where $\sqrt{\sigma_{11}(0)}$ and $\sqrt{\sigma_{22}(0)}$ are the maximum half-width and maximum half-angular divergence of the beam envelope at the extractor respectively, and $\sigma_{12}(0)$ is the correlation parameter between $\sigma_{11}(0)$ and $\sigma_{22}(0)$.

Hence, from eq.(5.1) and multiplying all the matrices together, $\sigma(z)$ becomes

$$\sigma(z) = \begin{pmatrix} A & B \\ -B & A \end{pmatrix} \tag{5.4}$$

where the submatrices

$$A = \begin{pmatrix} \sigma_{11}(0) + 2\sigma_{12}(0)\rho sin\frac{z}{\rho} + 2\sigma_{22}(0)\rho^2(1-cos\frac{z}{\rho}) & \sigma_{12}(0)cos\frac{z}{\rho} + \sigma_{22}(0)\rho sin\frac{z}{\rho} \\ \sigma_{12}(0)cos\frac{z}{\rho} + \sigma_{22}(0)\rho sin\frac{z}{\rho} & \sigma_{22}(0) \end{pmatrix}$$

and

$$B = \begin{pmatrix} 0 & -\sigma_{12}(0)sin\frac{z}{\rho} - \sigma_{22}(0)\rho(1-cos\frac{z}{\rho}) \\ \sigma_{12}(0)sin\frac{z}{\rho} + \sigma_{22}(0)\rho(1-cos\frac{z}{\rho}) & 0 \end{pmatrix}.$$

Therefore the maximum half-width, x_{max}, of the beam envelope in the x-plane as a function of axial distance is given by the square root of the matrix element σ_{11} of $\sigma(z)$. Hence

$$x_{max} = \left[\sigma_{11}(0) + 2\sigma_{12}(0)\rho sin\frac{z}{\rho} + 2\sigma_{22}(0)\rho^2(1 - cos\frac{z}{\rho})\right]^{1/2}. \tag{5.5}$$

The above expression also holds for the half-width of the beam envelope in the y-plane, as the beam is azimuthally symmetric.

The emittance, ϵ, of the beam at the extractor is defined as the area of the phase space ellipse occupied by the beam particles in the x-plane,

$$\epsilon = \pi\sqrt{\sigma_{11}(0)\sigma_{22}(0)(1 - r_{12}^2)} \tag{5.6}$$

where

$$r_{12} = \frac{\sigma_{12}(0)}{\sqrt{\sigma_{11}(0)\sigma_{22}(0)}}.$$

5.4 Emittance measuring device

As stated earlier, the emittance parameters $\sigma_{11}(0)$, $\sigma_{22}(0)$ and $\sigma_{12}(0)$ can be obtained from the beam envelope by measuring the beam profile at several axial positions. The measuring device consisted of a rigid and non-magnetic rotating probe, with seven 0.51 mm diameter tungsten wires each separated by 10 mm axially and 45° azimuthally. The azimuthal separation angle between the wires was large enough so that no more than one wire intercepted the beam at any rotation angle of the probe. In addition, a beam stop measured the extracted beam current. Figure 5.1 shows the emittance measuring device.

5.5 Experimental method

The emittance measuring device has been used to obtain the beam envelope of a 5 keV H^+ beam extracted from the ECR source employed in the TRIUMF OPPIS. The

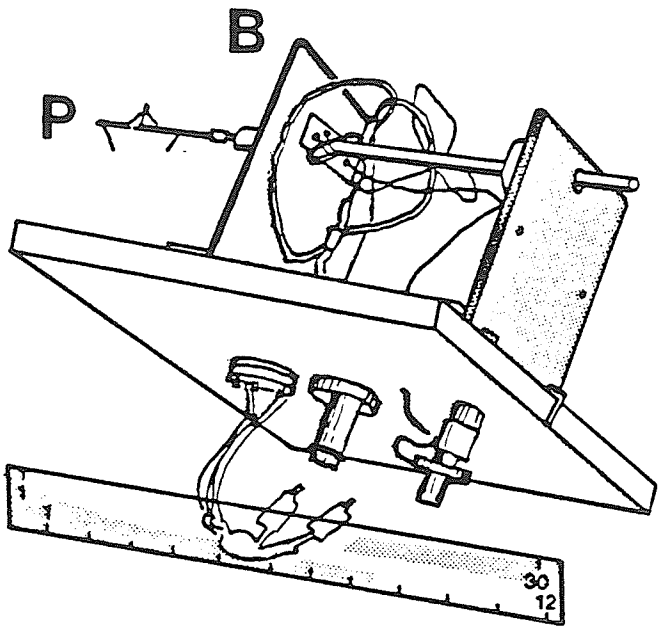

Figure 5.1: A schematic diagram of the emittance device. P: rotary probe with seven wires; B: beam stop.

extraction system of the ECR source was a three electrodes acceleration-deceleration type, as shown in fig 5.2. The aspect ratio S of the extraction system is given by $S = r/d$, where r is the aperture radius of the electrode and d is the first electrode gap.

In the measurements, the probe was inserted into the bore of the solenoid at a uniform 1.2 T magnetic field, and was offset from the beam axis by 12.7 mm (fig. 5.3). The wires and the beam stop were biased +45V to suppress secondary electrons produced by the incident ion beam. Current from the wires was fed into an electrometer and then to an X-Y chart recorder producing the beam profiles. By rotating the probe through a complete revolution, seven beam profiles corresponding to seven axial positions were produced. The half-widths of the beam envelope were obtained from the beam profile data as follows. The angular rotation of the probe was firstly calibrated, in terms of rad mm^{-1}, by measuring the length of the chart corresponding to a complete revolution of the probe. Then by measuring the half-widths at half-maximum (HWHM) of the profiles in mm from the chart, the half-widths of the modulated beam envelope, x_{max} in mm, of the beam at different axial positions downstream of the extractor were obtained according to

$$x_{max} = 12.7 sin\,[0.024(HWHM)] \tag{5.7}$$

where 12.7 mm was the offset distance between the beam axis and the probe axis, 0.024 rad mm^{-1} was the calibration factor for the angular rotation rate of the probe.

5.6 Application and results

Figure 5.4 shows an example of a beam profile scan and its corresponding beam envelope after transforming the HWHMs of the profiles into the half-widths of the beam envelope x_{max}. The profiles numbered in fig. 5.4(a) correspond to the x_{max} numbered in fig. 5.4(b). The profile #7 in fig. 5.4(a) corresponds to the x_{max} furthermost downstream of the beam envelope due to the location of the wire at the

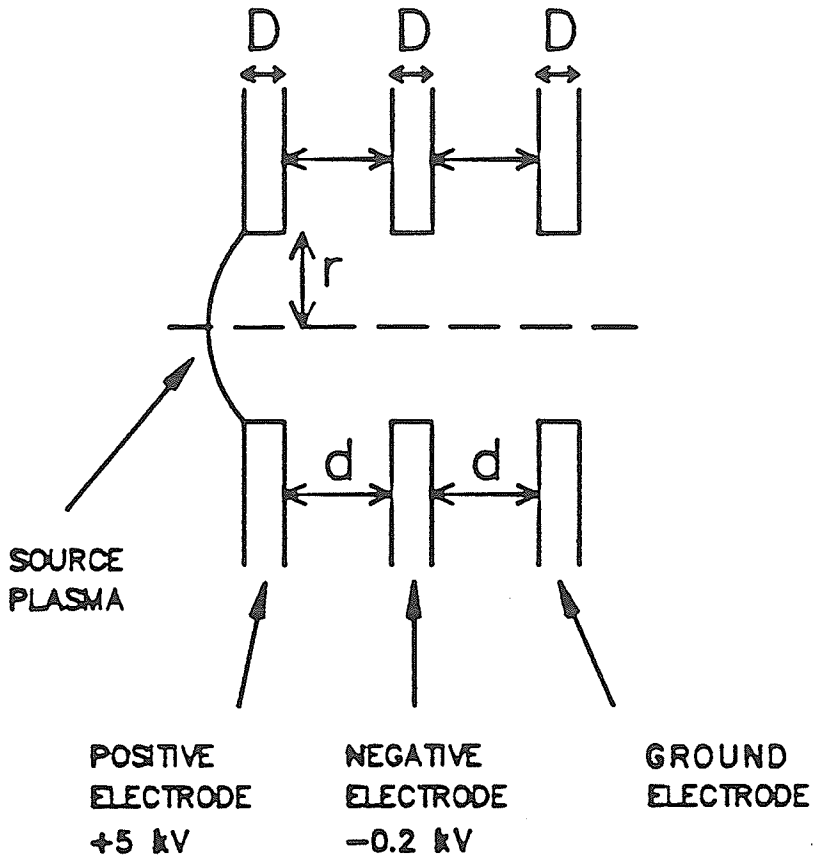

Figure 5.2: Dimensions of the extraction electrodes system used in the present work. The thickness of the electrodes $D = 0.8$ mm; the gap between electrodes $d = 3.0$ mm; the aperture radii of the electrodes r were varied from 0.5 mm to 1.75 mm. The aspect ratio $S = r/d$.

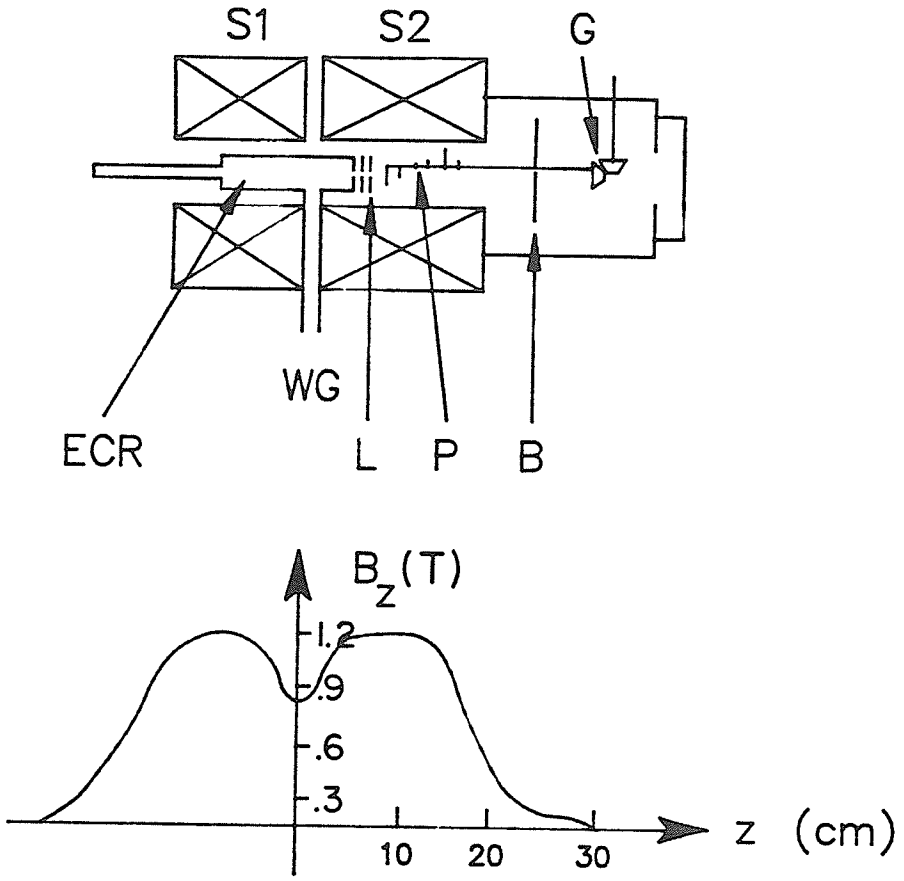

Figure 5.3: A schematic diagram showing the experimental setup. S1 and S2: solenoids; ECR: electron-cyclotron-resonance ion source; WG: waveguide for the ECR source; L: extraction electrodes; P: rotary probe; B: beam stop; G: gear to rotate the probe.

start of the probe rotation. The beam envelope has been corrected for the width of the wires. The different peak values and HWHMs of the profiles indicate the modulation of the beam size.

The profiles and the beam envelope obtained by this emittance measurement method may also be used to monitor the operation of the ECR source. The presence of residual gas impurities in the ECR plasma chamber or a poor vacuum inside the solenoid resulted in an increase of background level between the profiles. Also any mis-alignment of beam axis with the magnetic field axis would give a non-sinusoidal beam envelope.

As pointed out by Green [32] and Coupland and Green [33] theoretically and experimentally, the beam optics properties using a three electrodes acceleration-deceleration type extraction system are mainly determined by the conditions of the first gap. The variation of the beam emittance and brightness of an H^+ beam extracted from the TRIUMF ECR source has been measured as a function of the aspect ratio S of the extraction system (fig. 5.2) in two cases; namely, when the extraction system was located at a magnetic field strength $B = 0.9B_{max}$ and at $B = 0.99B_{max}$, where B_{max} was the 1.2 T magnetic field of the solenoid (fig. 5.3).

Throughout the investigation, the aperture radii of the electrodes were varied and the other conditions, which were the extractor gap, biasing potentials to the electrodes and magnetic field, were kept constant.

In order to ascertain the position of the extractor corresponding to $z = 0.0$ in eq.(5.5) in the least-sqaures fit of $(x_{max})^2$ against z/ρ to obtain the emittance parameters at the extractor, the beam envelopes have been traced back to the extractor region. As the extracted ion beam fills the aperture of the extractor, the ratio of the beam envelope width to the radius of the aperture, x_{max}/r, should remain constant at the extractor for different aperture radii. The standard deviation of the ratio x_{max}/r corresponding to all the radii of the extractor aperture has been calculated in the neighbourhood of the extractor region. If the extractor origin is correctly

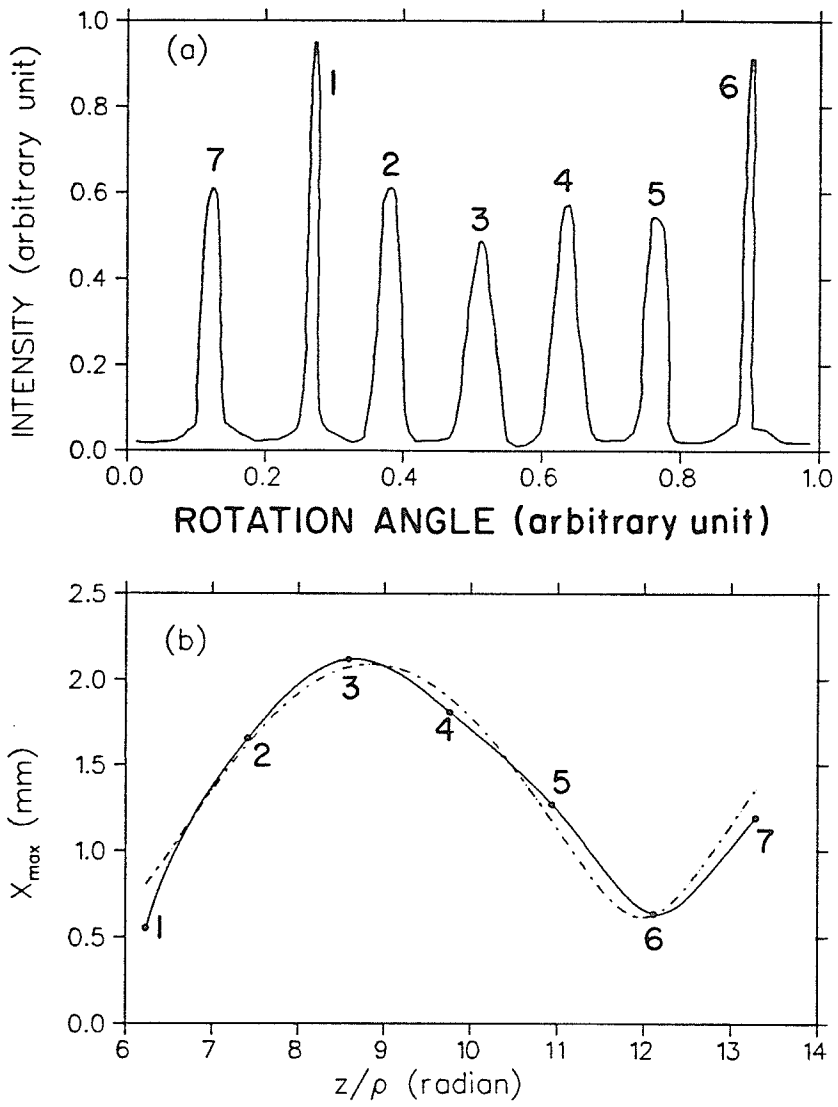

Figure 5.4: (a) An example of a beam profile scan recorded with a X-Y chart recorder. (b) The corresponding half-width of the beam envelope as a function of z/ρ; the solid curve is a cubic-spline fit to the measured x_{max} in data points; the broken curve is a least-squares fit to eq.(5.5).

identified at $z = 0.0$ in the least-squares fit of eq.(5.5), the standard deviation of x_{max}/r should be a minimum at the extractor position. In doing so, it has been found that, in the case where the extractor system was located at $B = 0.9B_{max}$, the minimum of the standard deviation of x_{max}/r for all radii is exactly at the extractor position, i.e. the position of the extractor has been correctly taken at $z = 0.0$ in the least-sqaures to $(x_{max})^2$ against z/ρ in eq.(5.5). However, in the case where the extractor was located at $B = 0.99B_{max}$, this minimum occurs at 2 mm upstream of the extractor, i.e. the correct extractor position has been offset by 2 mm in the measurements. This offset could arise from the measurement of the distance between the extractor and the wires of the probe, which picked up the beam profiles as a function of the axial distance z. To correct this offset, the emittance parameters have been obtained at the position where the minimum of the standard deviation of x_{max}/r occurs 2 mm upstream of the extractor in the measurements.

Tables 5.1 and 5.2 tabulate the emittance parameters and also the extracted beam current obtained by this emittance measurement method at different aspect ratios for the extraction system located at $B = 0.9B_{max}$ and at $B = 0.99B_{max}$ respectively. It should be noted that in the Table 5.2, the emittance parameters for r=0.5 mm (S=0.17) are not well determined due to the uncertainty in finding the minimum of the standard deviation of x_{max}/r close to the extractor region. The emittance is calculated using eq.(5.6) and corresponds to the 50% contour level of the total beam. The phase space ellipses at the extractor at different S are shown in fig. 5.5.

It is usual to define the normalized emittance ϵ_n by

$$\epsilon_n = \beta\gamma\epsilon \tag{5.8}$$

where β and γ are the usual relativistic factors for a 5 keV H^+ beam. One may also further define the normalized brightness, B_n, of the ion beam by

$$B_n = \frac{2f^2 I}{\epsilon_n^2} \tag{5.9}$$

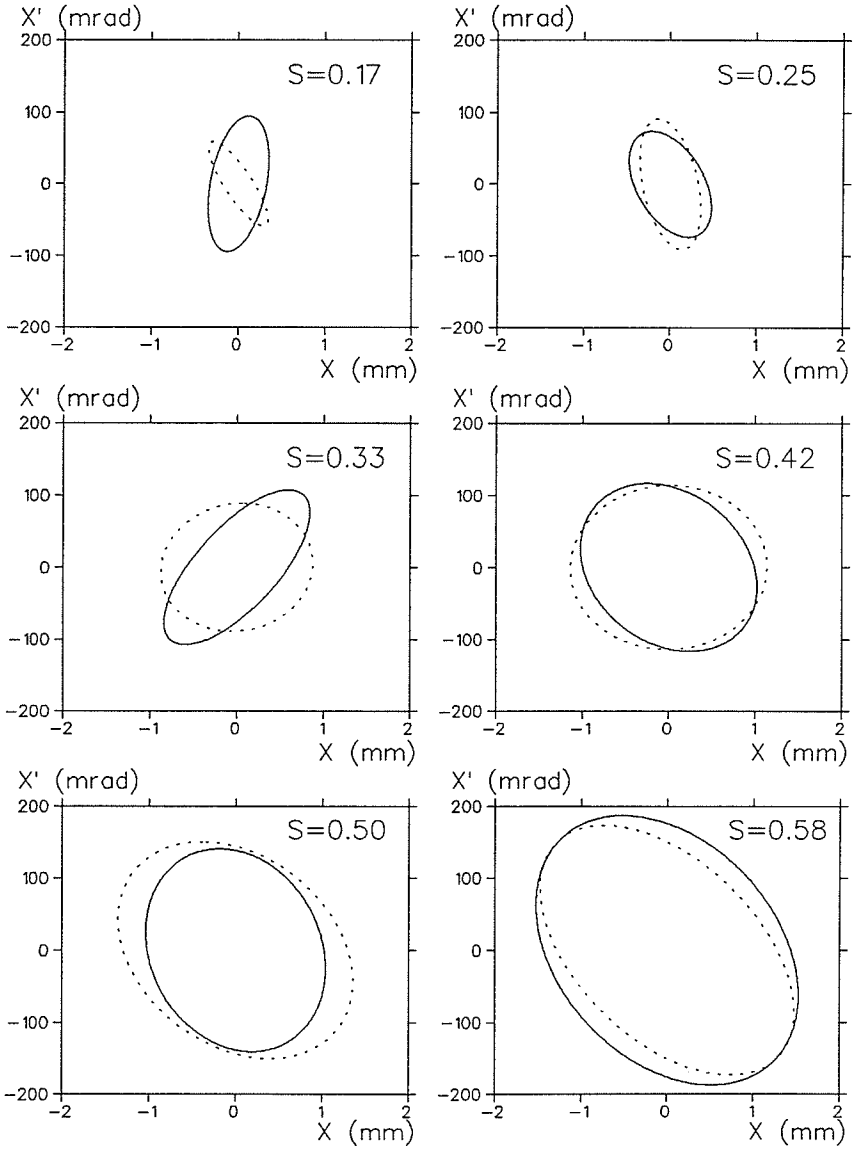

Figure 5.5: Phase space ellipses at the extractor for different aspect ratio S. Ellipses with solid curve: extraction system at $B = 0.9B_{max}$; ellipses with broken curve: extraction system at $B = 0.99B_{max}$.

Table 5.1: Tabulation of the emittance parameters and the extracted beam current at different aspect ratio for the extraction system at $B = 0.9B_{max}$.

Aperture Radius (mm)	S	Current (mA)	$\sigma_{11}(0)$ $(\text{mm})^2$	$\sigma_{12}(0)$ (10^1 mm-mrad)	$\sigma_{22}(0)$ (10^4 $(\text{mrad})^2$)	ϵ_n (π mm-mrad)
0.5	0.17	0.1	0.12	1.14	0.90	0.10
0.75	0.25	0.6	0.23	-1.57	0.54	0.10
1.0	0.33	1.7	0.70	6.39	1.15	0.21
1.25	0.42	2.0	1.04	-2.81	1.36	0.38
1.5	0.50	2.1	1.08	-2.64	1.98	0.47
1.75	0.58	2.5	2.32	-9.69	3.51	0.87

Table 5.2: Tabulation of the emittance parameters and the extracted beam current at different aspect ratio for the extraction system at $B = 0.99B_{max}$.

Aperture Radius (mm)	S	Current (mA)	$\sigma_{11}(0)$ $(\text{mm})^2$	$\sigma_{12}(0)$ (10^1 mm-mrad)	$\sigma_{22}(0)$ (10^4 $(\text{mrad})^2$)	ϵ_n (π mm-mrad)
0.5	0.17	0.03	0.12	-1.70	0.35	0.04
0.75	0.25	0.6	0.12	-1.25	0.83	0.10
1.0	0.33	1.5	0.77	0.51	0.79	0.25
1.25	0.42	2.0	1.29	0.16	1.30	0.42
1.5	0.50	2.4	1.83	-5.89	2.26	0.64
1.75	0.58	2.5	2.17	-12.79	3.01	0.72

where I is the extracted beam current measured by the beam stop, and f=0.5 is the fraction of the total beam within the $x - x'$ phase space ellipse emittance contour corresponding to the HWHM of the beam profiles [34].

Using the results from Table 5.1 and Table 5.2, the ratio ϵ_n/S and the normalized brightness B_n of the H^+ beam can be calculated and are shown in fig. 5.6 as a function of the aspect ratio S. For the case when the extraction system is located at $B = 0.9B_{max}$, the ratio ϵ_n/S has a minimum at $S \approx 0.25$ (fig. 5.6a). When the extraction system is located at $B = 0.99B_{max}$, $log(\epsilon_n/S)$ varies linearly with $log(S)$ with the slope of the straight line being $\sim$2 (fig. 5.6c). This linear dependence suggests that ϵ_n depends on S^3 in immersed flow beam dynamics. The maximum normalized brightness at $S \approx 0.25$ for both cases (fig. 5.6b and fig. 5.6d) shows that the TRIUMF ECR ion source should operate at this aspect ratio in order to deliver a high brightness H^+ beam.

It is interesting to note that the average of the ratio x_{max}/r at the extractor is $\sim$0.73 for all the radii of the extractor aperture used in the present work. This ratio has an interpretation as the fraction of the total beam within the $x - x'$ phase ellipse emittance contour, and is equivalent to f (taken to be 0.5) corresponding to the HWHM approximation in the calculation of the normalized brightness (eq.(5.9)). Therefore the normalized brightness of the extracted H^+ beam, presented in fig: 5.6, has been underestimated if f should be 0.73 in immersed flow beam dynamics.

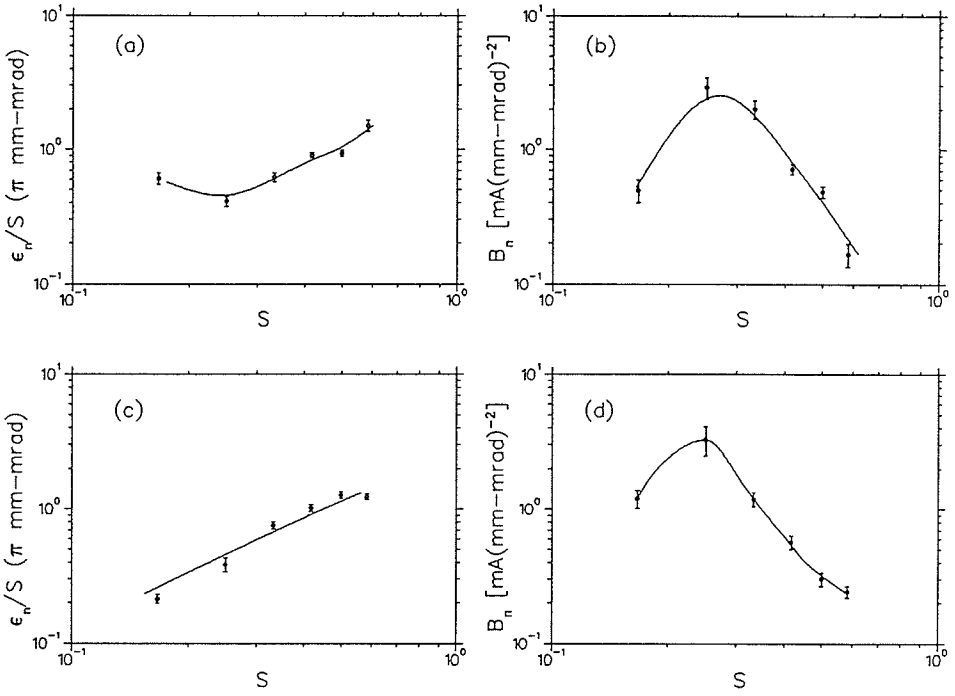

Figure 5.6: (a) and (b) Measured ϵ_n/S and B_n as a function of S for the extraction system located at $B = 0.9B_{max}$. (c) and (d) Measured ϵ_n/S and B_n as a function of S for the extraction system located at $B = 0.99B_{max}$. The curves are the smooth curves to the data points.

Chapter 6

Emittance Growth of H^- Beam From $H^0 \longrightarrow H^-$ In a Solenoid

6.1 Overview

In the operation of any type of polarized ion source, ionization of a nuclearly polarized neutral atomic beam is carried out in an axial magnetic field in order to preserve the nuclear polarization. Ohlsen et al. [6] have predicted the emittance degradation of an atomic beam ionized by charge exchange in a solenoidal magnetic field and have calculated that the effective emittance growth ($\Delta\epsilon$) as the beam leaves the fringe field is given by

$$\Delta\epsilon = \frac{\pi r^2}{2\rho} \tag{6.1}$$

where $\rho = \frac{mv_z}{qB_z}$, q/m is the charge-mass ratio of the ion, B_z is the axial magnetic field in the ionizer region, r is the radius of the beam envelope in the ionizer and v_z is the axial velocity of the ion beam.

It is of importance to measure the emittance of the H^- beam and then to verify the validity of the above equation as applied to the OPPIS at TRIUMF. The emittance is a fundamental parameter important in the design of the ionizer as well as in the H^- beam optics required for transporting the H^- beam to the accelerator.

6.2 Derivation and justification of ($\triangle\epsilon$)

In deriving the above equation, it is assumed that a particle travels with velocity v_z parallel to the axis of the solenoidal magnetic field, and is then ionized inside the solenoid at a radius r from the beam axis. From the impulse approximation of the field gradient, v_z is assumed to be large compared to any additional velocity components which are acquired as the particle leaves the solenoidal field after ionization. Furthermore, the particle, which is ionized at the radius r, remains at the same radius when leaving the fringe field. Therefore the trajectory of the particle in the solenoid is considered to be a straight line for the purpose of estimating the velocity change. The force on the particle is given by the Lorentz force

$$\mathbf{F} = m\frac{d\mathbf{v}}{dt} = q\mathbf{v} \times \mathbf{B}, \tag{6.2}$$

where m is the particle mass, B is the magnetic field vector, and $\mathbf{v}$ is the particle velocity vector. Since only the z component of $\mathbf{v}$ is assumed to be non-zero, eq.(6.2) reduces to

$$m\frac{dv_\theta}{dt} = qv_zB_r \tag{6.3}$$

where B_r is the radial component of $\mathbf{B}$ and v_θ is the azimuthal component of $\mathbf{v}$. Substituting $v_z\frac{d}{dz}$ for $\frac{d}{dt}$ and integrating over the path of the particle, v_θ is obtained as

$$v_\theta = \frac{q}{m}\int_z^\infty B_r(z)dz. \tag{6.4}$$

However, by Gauss' theorem,

$$2\pi r\int_z^\infty B_r(z)dz = \pi r^2 B_z \tag{6.5}$$

where B_z is the uniform magnetic field in the ionizing region. Substituting eq.(6.5) into eq.(6.4), v_θ becomes

$$v_\theta = \frac{q}{2m}B_z r, \tag{6.6}$$

which shows that an angular velocity is imparted to the off-axis particle when the particle is leaving the solenoidal field.

The quantity of interest is the effective emittance growth ($\triangle\epsilon$) given by

$$\triangle\epsilon = \pi v_\theta \frac{r}{v_z} = \frac{\pi r^2}{2\rho} \tag{6.7}$$

which is eq.(6.1).

6.3 Emittance measurement and results

In the OPPIS at TRIUMF, the H^- beam is produced by charge exchange of an atomic H^0 beam in an alkali vapour cell located in a solenoid. The trajectories for off axis H^- particles are defocussed due to the radial component B_r in the fringe field of the solenoid. Hence, a significant divergence, which depends on the radius at which particles are ionized, is imparted to the beam upon leaving the solenoid. Although there is no increase in the volume of the 4-dimensional transverse phase space occupied by the beam particles (in accordance with Liouville's theorem), there is an increase in the projection on the $x - x'$ or the $y - y'$ transverse phase space plane, i.e. effective emittance growth of the beam in the transverse plane.

The purpose of the present work was to measure the emittance of the H^- beam (5 keV energy) produced in the TRIUMF OPPIS as a function of the ionizer magnetic field.

The H^- beam emittance was measured with a Los Alamos type slit scanner [35] placed 500 mm downstream of the ionizer solenoid (fig. 6.1). Figure 6.2 shows schematically the scanner and the trajectory of an H^- particle. The scanner was driven across the beam in a transverse direction, X. The divergence angle X', at which the H^- ions enter the scanner and are then deflected by the pair of deflecting plates through the second slit into the Faraday cup, is given by

$$X' = \frac{1}{4}\frac{L}{S}\frac{V_p}{V_b} \tag{6.8}$$

where L and S are the length and separation of the deflecting plates respectively, V_p is the ramped potential applied to the plate and V_b is the potential of the H^-

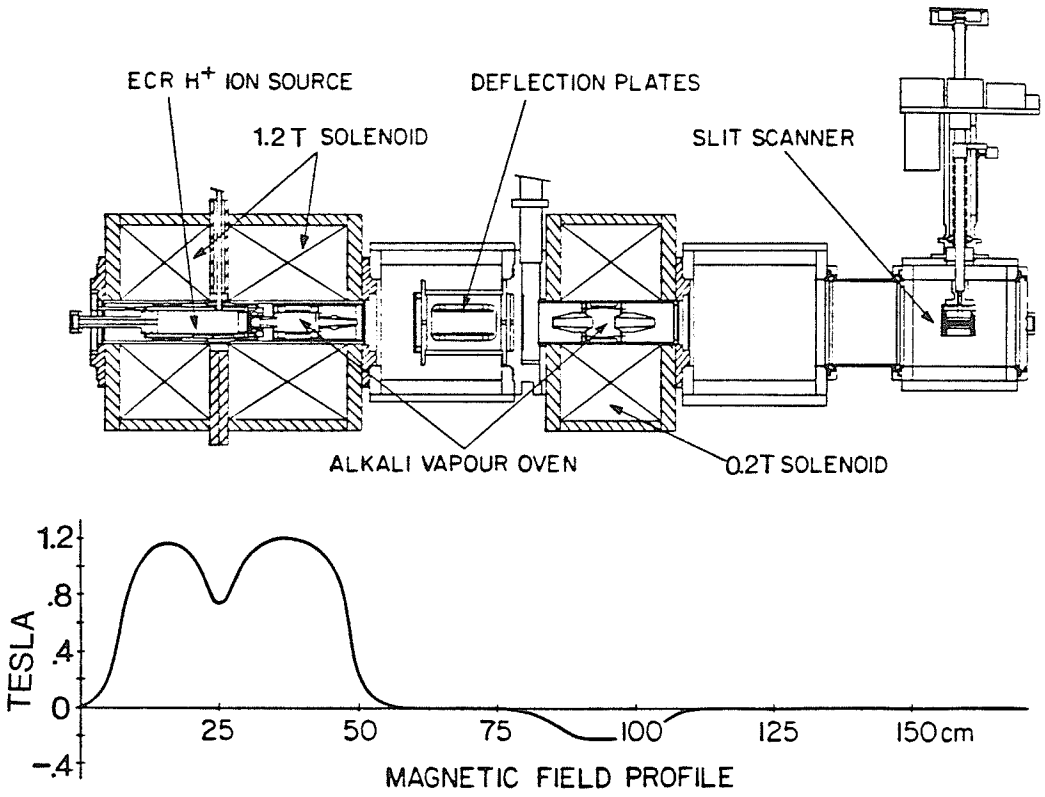

Figure 6.1: A schematic diagram showing the TRIUMF OPPIS and the position of the Los Alamos slit scanner used in the measurements of the emittance of the H^- beam. The magnetic field profile along the beam axis is shown in the lower part of the diagram.

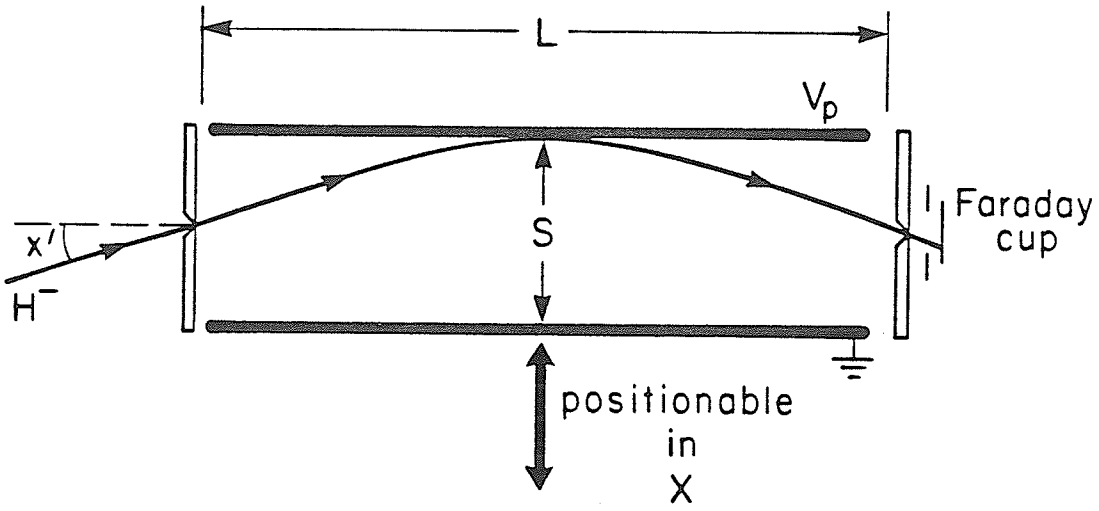

Figure 6.2: A schematic diagram showing the Los Alamos type slit scanner and a H^- ion trajectory through the scanner.

beam. For every position in the beam (X), a curve of beam intensity versus the angle (X') is generated. A three-dimensional view of the beam in phase space is obtained. Taking a slice parallel to the $X - X'$ plane produces a contour, which is labelled by the percentage of the measured current within this contour. The area enclosed by the contour is the emittance for the $X - X'$ plane. An example of a measured emittance at a 0.1 T ionizer field is shown in fig. 6.3 for several emittance contours. For the contour containing the highest percentage of the beam, two different emittances are observed. In addition to the 5 keV H^- beam there is also a small 2.5 keV H^- component resulting from 5 keV H_2^+ produced by the proton ion source. The analysis of emittance growth has been at a 60% contour level where the contribution from H^- resulting from the H_2^+ component is negligible.

The normalized emittance growth $(\triangle\epsilon)_n$ of the H^- beam is defined by

$$(\triangle\epsilon)_n = \beta\gamma(\triangle\epsilon) \tag{6.9}$$

where β and γ are the usual relativistic factors for a 5 keV H^- beam and $(\triangle\epsilon)$ is given by eq.(6.1). The dependence of the normalized emittance as a function of ionizer fields is shown in fig. 6.4 for the 60% contour level. The aperture radius of the ionizer used in the $H^0 \longrightarrow H^-$ charge exchange was 6 mm and the beam envelope radius corresponding to the 60% contour level is therefore 3.6 mm. Using eq.(6.9), the slope of the straight line in fig. 6.4 implies a beam radius of (3.6±0.2) mm. It is therefore concluded that the theory of Ohlsen et al. correctly describes the observed emittance growth of the H^- beam as a function of the ionizer field. The intercept at the vertical axis in fig. 6.4, which is 0.07π mm-mrad, is due to the normalized emittance of the H^0 beam accepted by the ionizer, and the emittance growth due to the scattering during charge exchange. The acceptance of the ionizer for the H^0 beam has been estimated to be 0.078π mm-mrad at the 60% contour level. Thus the emittance growth resulting from scattering is negligible.

In summary, the transverse emittance of the H^- beam in the OPPIS at TRIUMF has been measured and found, under its operating conditions, to be linearly

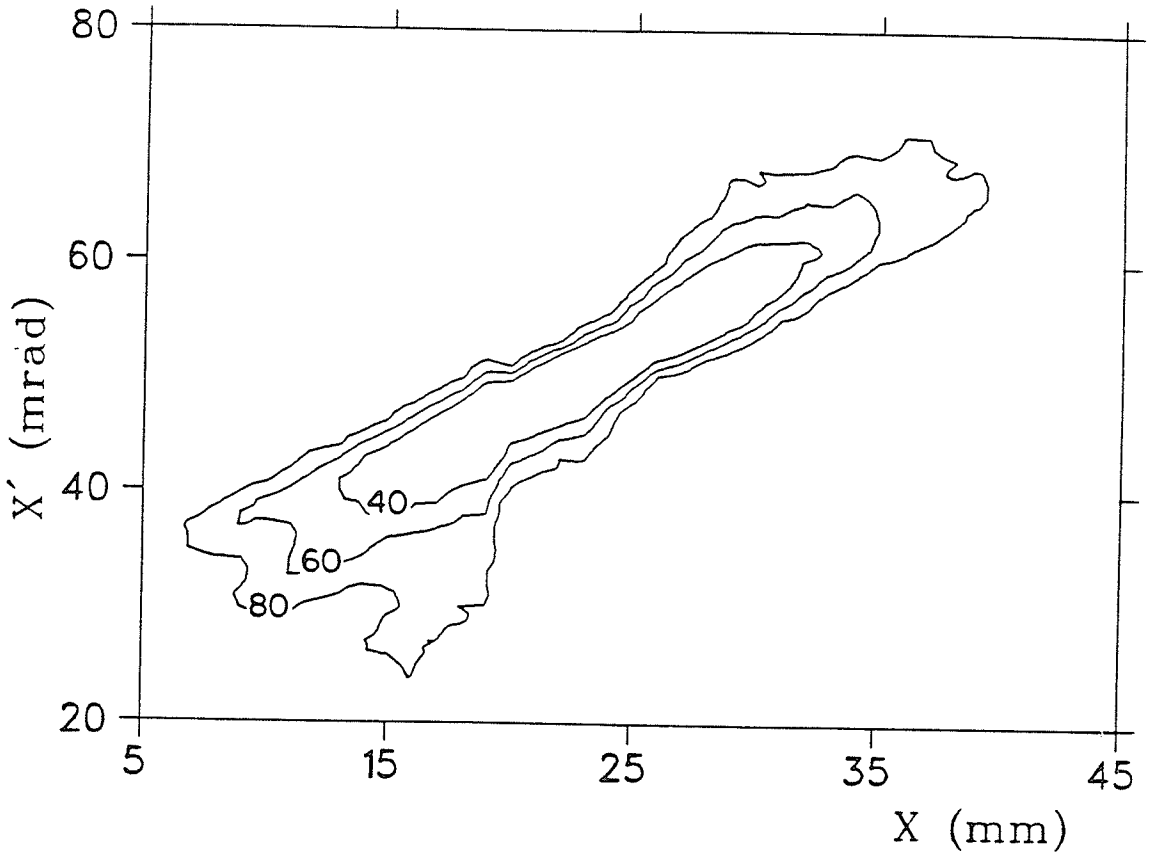

Figure 6.3: Emittance contours for the H^- beam with 0.1 T ionizer field. Contour labels represent the percentage of the total beam within the contours.

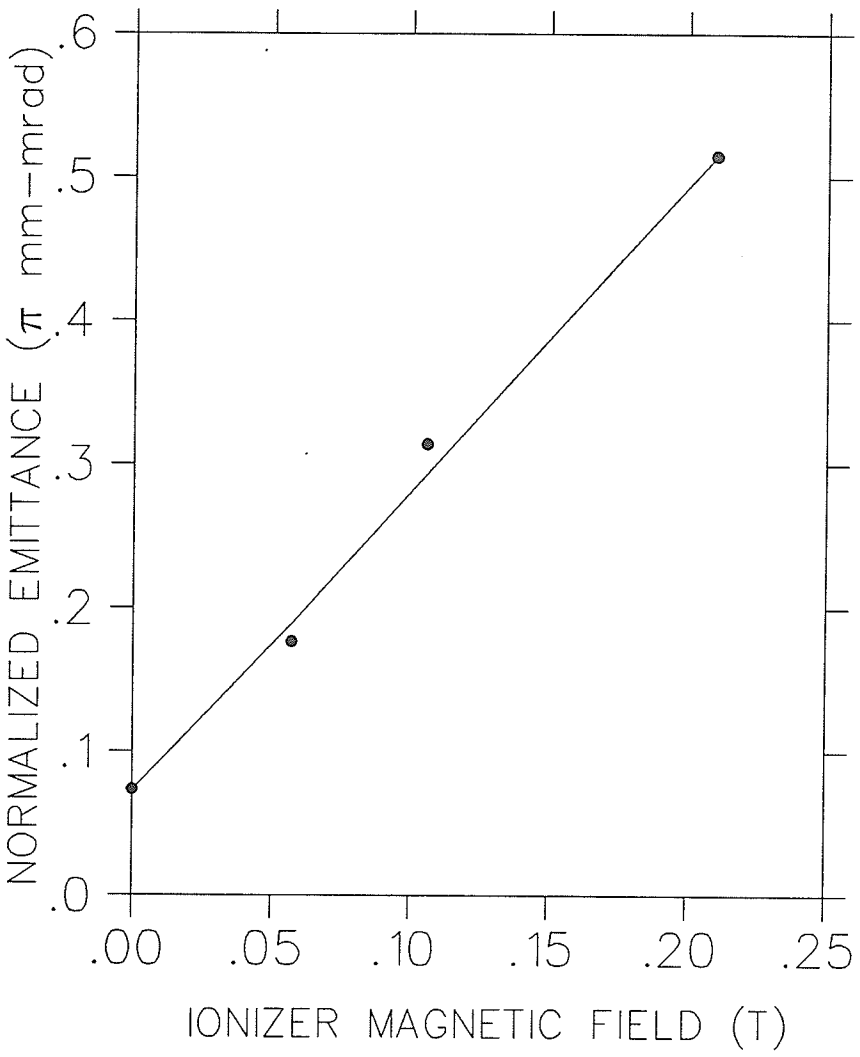

Figure 6.4: Measured normalized emittance of H^- beam as a function of the ionizer magnetic field at a 60% contour level of the total beam. The straight line is the least-squares fit to the data points.

dependent on the ionizer magnetic field in agreement with the theory of Ohlsen et al.

Chapter 7

Beamline Design

7.1 The beamline

A beamline with electrostatic focussing elements is needed to transport the 5 keV H^- beam exiting from the ionizer of the OPPIS to the accelerating column of the 300 keV injection beamline for the TRIUMF cyclotron. The design criteria for the beamline are compactness and mininum beam loss. Two spherical 45° electrostatic bends are used to separate the H^- beam from the unwanted H^0 beam. A spin rotator is needed to rotate the nuclear spin of the H^- beam by $\pi/2$ from horizontal to vertical direction so that the spin direction is parallel or anti-parallel to the cyclotron magnetic field. Two einzel lenses are used to focus the H^- beam into the spin rotator and into the accelerating column. Some correcting plates are also used to steer the beam horizontally and vertically. The beamline together with the source mounted onto the HV terminal is shown schematically in fig. 2.1. In this chapter, some significant design characteristics and operating parameters of these focussing elements are presented.

7.2 Spin rotator design aspects

7.2.1 Calculation of the magnetic and electric field strengths

The direction of the nuclear spin of the H^- ions from the OPPIS is longitudinal. In order that the spin direction is parallel or anti-parallel to the cyclotron magnetic field, the spin must be rotated by $\pi/2$. A Wien filter is a device which consists of crossed electric and magnetic fields such that the particle trajectory is unaffected by the fields, but the magnetic field rotates the spin direction. It is therefore neccessary to calculate the magnitudes of the fields.

In general, the rate Ω at which the spin of a particle precesses in a uniform electrogmagnetic field is given by the Bargmann-Michel-Telegdi (BMT) equation [37]

$$\Omega = \frac{e}{m}\{(\mathbf{E}\cdot\hat{\mathbf{n}}/v)[(\frac{g}{2}-1)-\frac{g}{2\gamma^2}]+(\hat{\mathbf{v}}\cdot\mathbf{B}\times\hat{\mathbf{n}})(\frac{g}{2}-1)\} \tag{7.1}$$

where $\hat{\mathbf{n}}$ is the unit normal vector of the unit velocity vector $\hat{\mathbf{v}}$; $\mathbf{B}$ and $\mathbf{E}$ are the magnetic and electric field vectors respectively; γ is the usual relativistic factor; g is the g-factor and e/m is the charge-mass ratio of the particle.

In a Wien filter, the $\mathbf{B}$, $\mathbf{E}$ and $\mathbf{v}$ are orthogonal to each other. The BMT equation reduces to

$$\Omega = \frac{g}{2}\frac{e}{m}\frac{B}{\gamma^2}. \tag{7.2}$$

Ω is given by $\frac{d\theta}{dt}$ where θ is the angle of precession. The Wien filter has length of l so that $dt = \frac{dl}{v}$. Hence,

$$v\frac{d\theta}{dl} = \frac{g}{2}\frac{e}{m}\frac{B}{\gamma^2}. \tag{7.3}$$

For spin rotation of $\pi/2$,

$$Bl = \frac{v\pi}{g}\frac{m}{e}\gamma^2. \tag{7.4}$$

Applying the above equation to the spin precession of protons from the longitudinal to transverse direction (the g-factor is 5.58 for proton) and for a velocity corresponding to a 5 keV proton beam, it is found that $Bl = 0.0057$ Tesla-m.

The length of the Wien filter is 0.1 m, therefore the magnitude of the uniform magnetic field is 0.057 T.

Since $\mathbf{E} = -\mathbf{v} \times \mathbf{B}$ and $\mathbf{v} \perp \mathbf{B}$, the corresponding electric field strength of the Wien filter is therefore 557 Vcm^{-1}.

7.2.2 Focussing properties of a Wien filter

In the design of a Wien filter, its optical properties should also be examined. As the $\mathbf{E}, \mathbf{B}$ and $\mathbf{v}$ are all orthogonal to each other in a Wien filter, their vector components are given as $\mathbf{B} = B_y$, $\mathbf{E} = E_x$, and $\mathbf{v} = v_z$ is the beam velocity along the beam direction z, where x and y are the two transverse directions.

It has been shown [38] that the equations of motion, expressed in matrix form, of the H^- beam in the x and y direction of the Wien filter are given as

$$\begin{pmatrix} x \\ x' \end{pmatrix} = \begin{pmatrix} cos(kl) & k^{-1}sin(kl) \\ -ksin(kl) & cos(kl) \end{pmatrix} \begin{pmatrix} x_0 \\ x'_0 \end{pmatrix} \tag{7.5}$$

and

$$\begin{pmatrix} y \\ y' \end{pmatrix} = \begin{pmatrix} 1 & z \\ 0 & 1 \end{pmatrix} \begin{pmatrix} y_0 \\ y'_0 \end{pmatrix} \tag{7.6}$$

where l is the length of the Wien filter, x_0 and x'_0 are the initial position and divergence respectively in the x-direction of the beam at the entrance of the Wien filter, and similarly for y_0 and y'_0 in the y-direction, $k = E_x/2V_0$ where E_x and V_0 are the electric field strength (577 Vcm^{-1}) of the Wien filter and the potential of the H^- beam (5 kV) respectively.

The equations in the x-direction, i.e. along the electric field vector direction, are the same as those for the converging part of a magnetic quadrupole lens. Therefore the beam is focussed along the electric field vector direction but drifts along the magnetic field vector direction (y-direction) in the Wien filter.

The focal length of the Wien filter in the electric field vector direction is given

by

$$f = [ksin(kl)]^{-1} \tag{7.7}$$

For the geometry of the Wien filter (l = 10 cm) and for a 5 keV H^- beam in the OPPIS, the focal length along the direction of the electric field vector in the Wien filter is therefore about 32 cm.

7.3 Einzel lens design aspects

A pair of einzel lenses of focal lengths 10 cm and 18 cm are used to focus the H^- beam. Their geometries were designed by using computer codes RELAX3D [39] and TRIWHEELRE [40]. The potential distribution ϕ of the lens was firstly numerically calculated by solving the Laplace equation with Dirichlet condition in cylindrical coordinates (r, z),

$$\nabla^2 \phi(r, z) = 0 \tag{7.8}$$

where z is the longitudinal direction and r is the radial direction, with the over-successive-relaxation numerical method employed in RELAX3D. The output of the potential distribution was stored in an external computer file.

By recalling the potential distribution calculated by RELAX3D, the computer code TRIWHEELRE then traced the H^- trajectory through the lens by numerically integrating the equations of motion in (r, z) coordinates with the Runge-Kutta numerical method. The outer electrodes of the lens were grounded while the inner electrode was positively biased. For a 5 keV H^- ion with trajectory parallel to the beam axis at a height r_0 into the lens, the focal length f of the lens can be calculated according to

$$f = -\frac{r_0}{(r')_{z=l,r=0}} \tag{7.9}$$

where r' is the slope of the trajectory of the particle crossing the beam axis at $z = l$.

For convenient machining and assembly of the two lenses, both lenses have the same geometry, as shown in fig. 7.1.

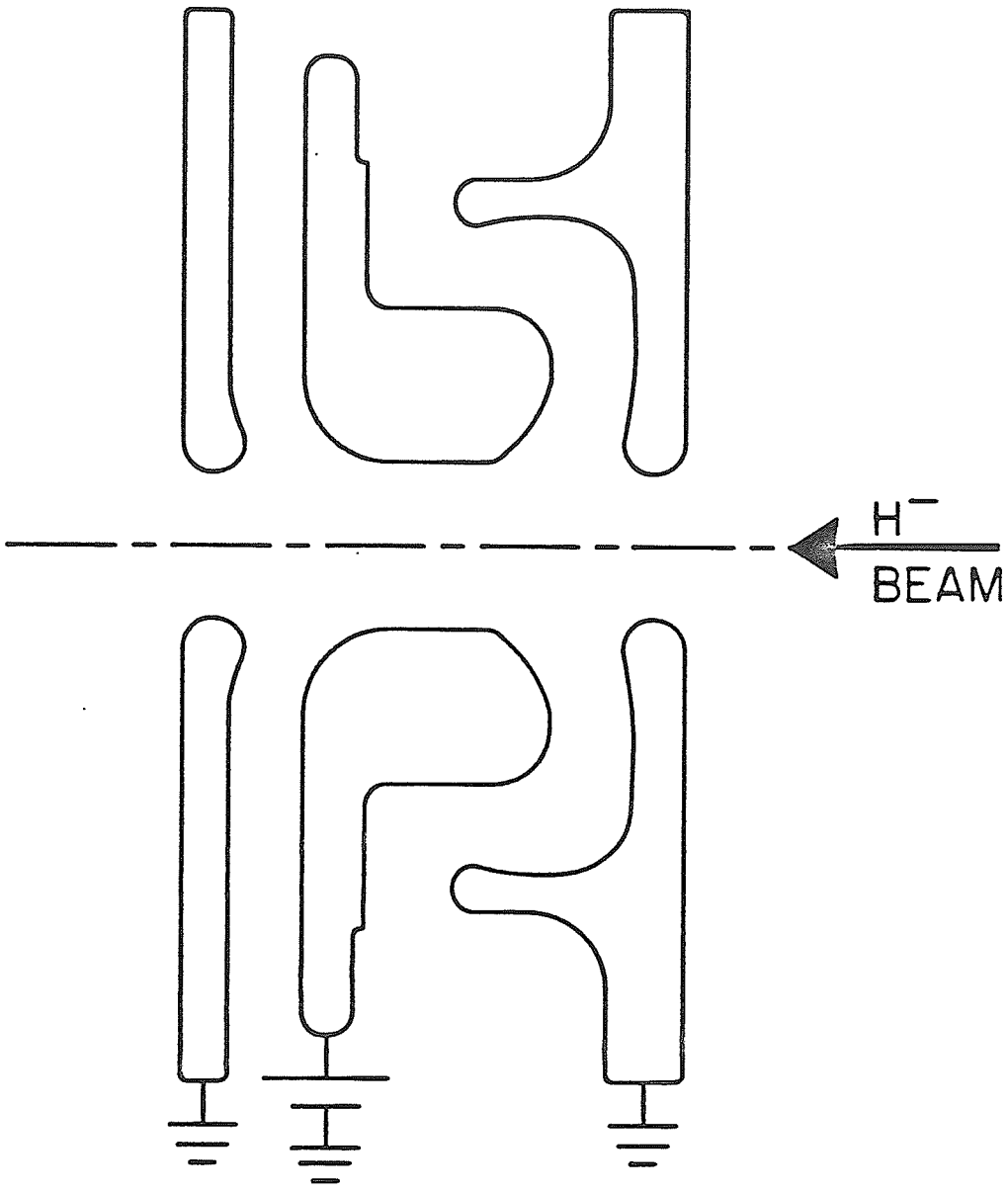

Figure 7.1: The geometry of the einzel lens used in the transport beamline of the OPPIS at TRIUMF, showing full scale of the lens.

It was found that the focussing power ($= f^{-1}$) of the lens increased with increasing biasing potential of the inner electrode. In order to have focal lengths of 10 cm and 18 cm, the inner electrodes of the two lenses have to be biased $\approx +10$ kV and $+8$ kV respectively. The variation of the focal length of the lens as a function of the height r_0 of an H^- particle incident parallel to the beam axis is shown in fig. 7.2 for different biasing voltage of the lens. As seen in this graph, the focal lengths of the lens change less than 5% for $r_0 \leq 5$ mm, which is about the radius of the H^- beam incident on the lens.

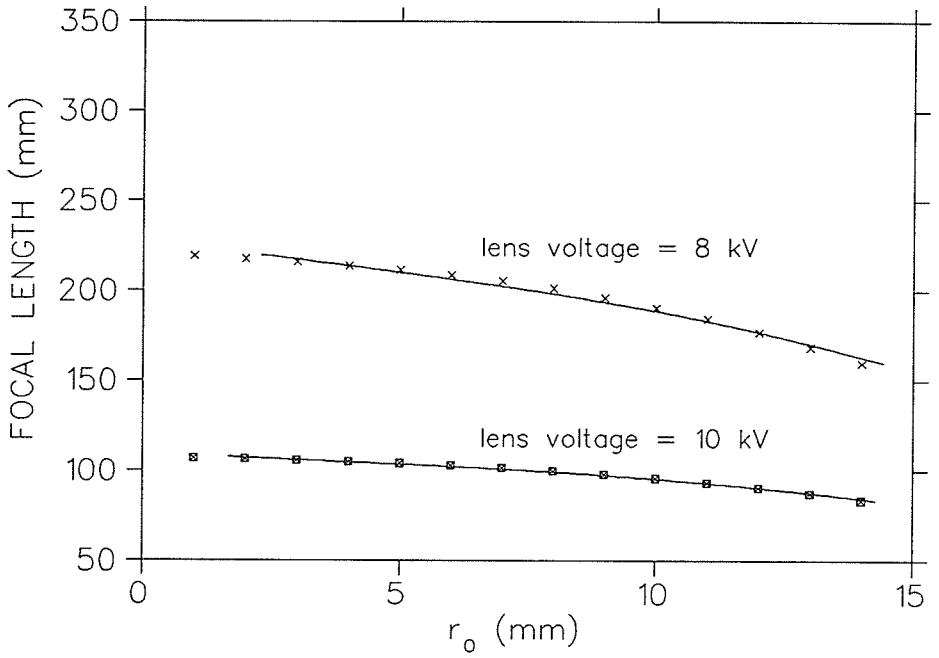

Figure 7.2: Variation of the focal length of the einzel lens for a 5 keV H^- beam as a function of r_0 at different biasing potentials.

Chapter 8

Initial Commissioning Experience And Future Research On The TRIUMF OPPIS

8.1 Initial commissioning experience

Maximum H^- current measured in front of the 300 kV acceleration column was about 13 μA at a sodium target thickness $>10^{14}$ atoms cm^{-2} in the neutralizing cell. Typical current at a more usual thickness of 2-3$\times10^{13}$ atoms cm^{-2} was $\sim$1 μA, with half that accelerated to 290 MeV.

Figure 8.1(a) shows the nuclear polarization of the proton beam at 290 MeV and the atomic polarization of sodium at 1.2 T magnetic field as a function of the sodium thickness for a single experimental run. The sodium polarization was limited by laser transmission losses in the argon gas cell (fig. 2.3). A sodium polarization of 87% at a thickness of 2.9$\times10^{13}$ atoms cm^{-2} was produced with the argon cell removed. The solid curve in fig. 8.1(b) shows the ratio of the nuclear polarization of the proton beam to the atomic polarization of the sodium vapour. The fall in this ratio at low sodium thickness is due to the background hydrogen neutralization. The extracted beam current increases with hydrogen gas to the ECR plasma chamber, while the proton polarization decreases due to the neutralization. At high sodium thickness, the ratio rises to 80%, which is close to the theoretical limit calculated

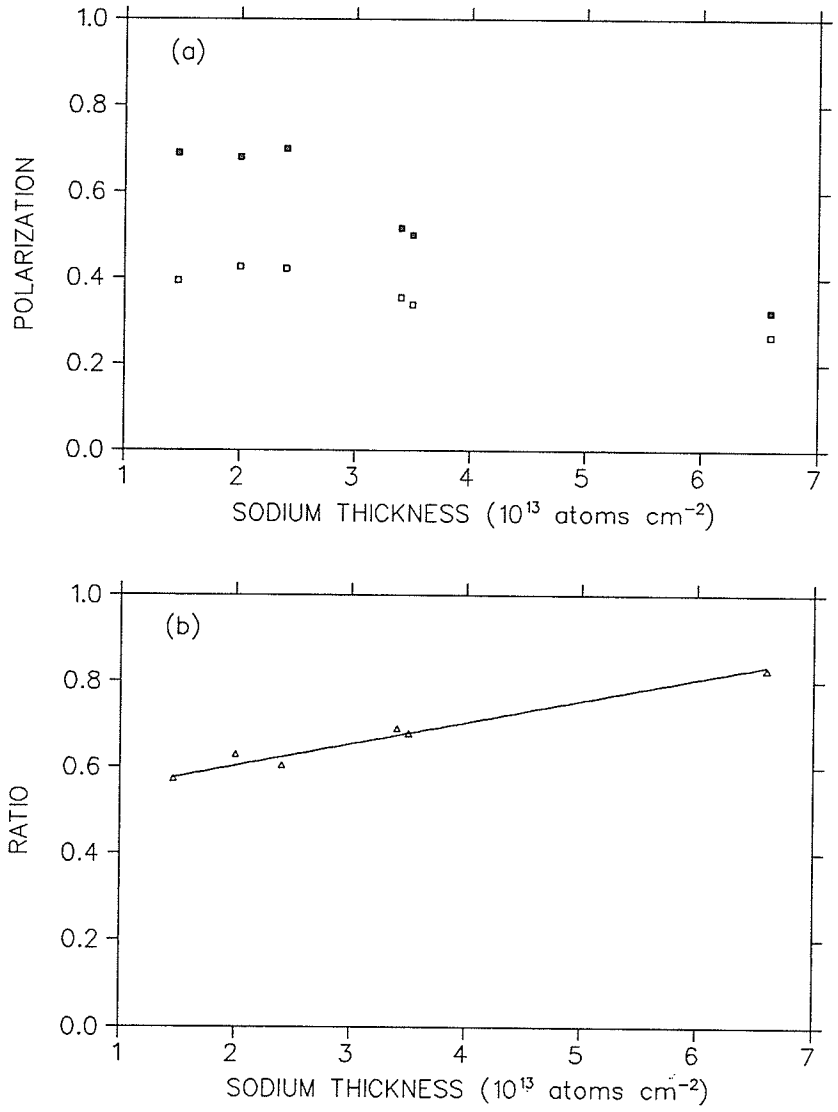

Figure 8.1: (a) The nuclear polarization of the proton beam at 290 MeV (open squares) and the sodium atomic polarization (solid squares) as a function of sodium thickness. (b) The solid curve is a least-squares fit for the ratio (triangles) of the proton polarization to the sodium atomic polarization.

by Hinds et al. [14] for a 1.2 T field in the sodium neutralizing cell region.

The nuclear polarization of the proton beam is flipped at rates up to 100 Hz as the result of flipping the helicity of the pumping laser beam through a Pockels cell, to which an external voltage is applied (see fig. 2.3). A test on the intensity of the proton beam has been made [36] when the nuclear polarization of the proton beam was flipped. This was done by digitizing the signal from a beam current measuring ionization chamber as a function of time following spin flip. Figure 8.2 shows the intensity of the signal when the nuclear polarization of the proton beam was flipped in up, down and off state. The intensity changes between the polarized and unpolarized states of the proton beam. When the Na atoms in the neutralizing cell are polarized, any H^0 neutrals formed, by charge exchange of the H^+ ions with the polarized Na atoms, are less likely to undergo a second charge exchange with the polarized Na atoms due to the Pauli exclusion principle, resulting in a higher intensity of polarized H^- beam from the OPPIS. However, between the up and down states, no change in beam intensity can be observed at a level of 0.1%, showing the stability of the proton current after flip.

8.2 Future research

Immediate and future efforts are to improve the brightness and polarization of the H^- beam. A superconducting solenoid will be used to replace the conventional solenoid in the ECR source, and will increase the magnetic field in the sodium neutralizer cell region to 2.5 T. This will increase the polarization transfer efficiency from 80% to ~95% [14].

In addition, the inner diameter of the bore of the superconducting solenoid will be twice of that of the present conventional solenoid, thus greatly improving the vacuum pumping and hence reducing the background hydrogen gas. The use of the superconducting solenoid also allows an assembly of permanent sextupole magnets

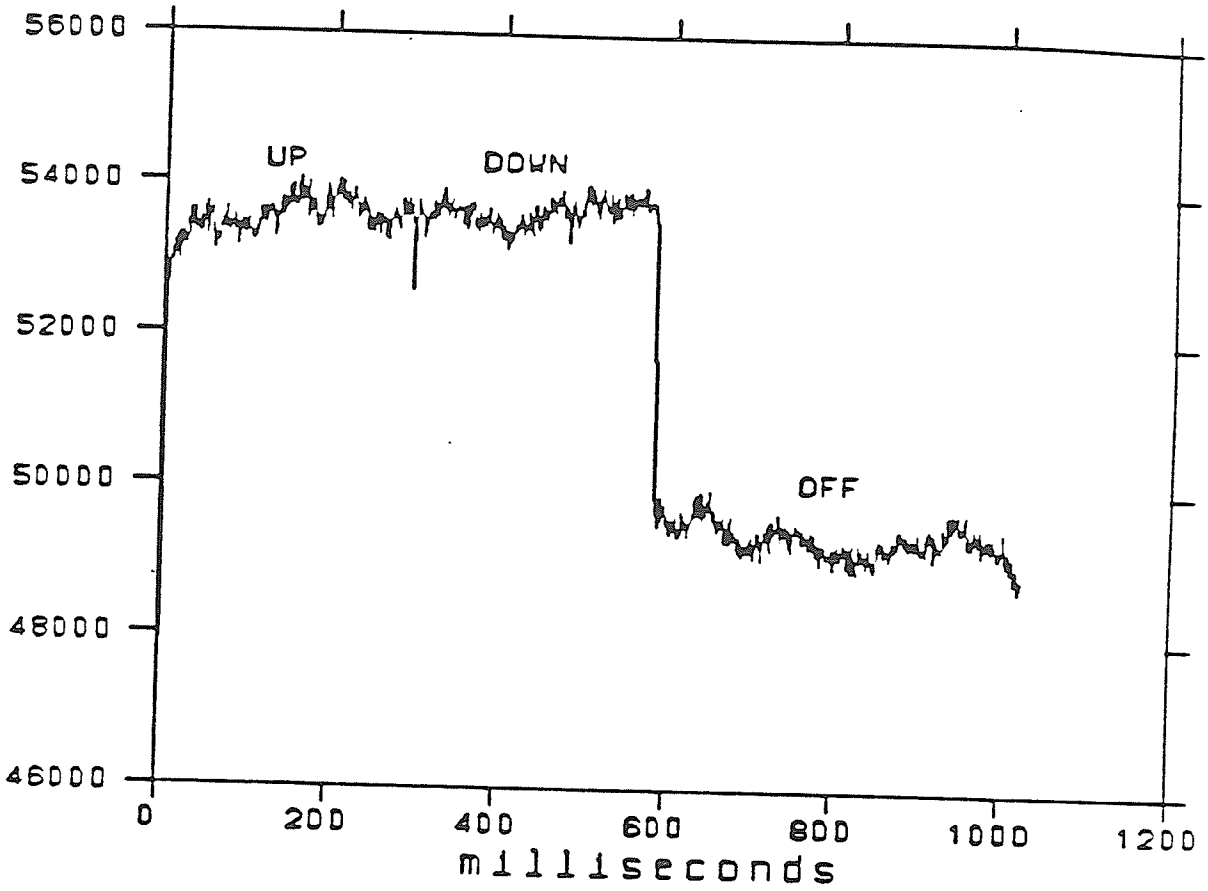

Figure 8.2: Beam current as a function of time following spin flip. The energy of the proton beam was 290 MeV.

to be installed inside the ECR source chamber. The use of a strong axial mirror and a multipole radial magnetic field in the ECR source has been known [26] to increase the confinement of the plasma density in the ECR chamber, and therefore to increase the brightness of the extracted H^+ beam.

The high axial magnetic field (2.5 T) produced by the superconducting solenoid will also increase the wall relaxation time of the sodium atoms (see chapter 3), and hence increase the steady state polarization of the sodium vapour.

An important effect in the optical pumping of the alkali vapour is the trapping of the pumping light. Trapping occurs when the vapour is sufficiently dense ($\sim 10^{14}$ atoms cm^{-2}) that multiple scattering of the light is important for one or more radiative decay branches of the vapour, therefore limiting the atomic polarization of the alkali vapour achievable by optical pumping. Tupa and Anderson [20] have theoretically shown the limitations imposed by radiation trapping on the atomic polarization in an alkali vapour by optical pumping in a large magnetic field, and found that atomic polarizations of 90% are possible with sodium thicknesses up to 10^{14} atoms cm^{-2} in a large magnetic field. Recent experimental results by Mori et al. [41] show a rapid relaxation rate due to the effect of radiation trapping in optically pumped sodium atoms at a thickness $\sim 10^{14}$ atoms cm^{-2}. Experimental work should be carried out to investigate the degradation of sodium polarization due to radiation trapping.

Search for suitable wall coating materials to prolong the wall relaxation time of sodium atoms should be continued. Such materials are of low local magnetic field and are not destroyed by the incident H^+ beam. The geometry of the neutralizer cell should be long enough to minimize the effusion of polarized atoms through the apertures at both ends of the cell, and the inner diameter of the cell is slightly greater than the size of the envelope of the incident H^+ beam. The pumping laser beam must fill the neutralizer cell so that only polarized electrons are captured by the H^+ beam.

In general, further research on the OPPIS remains in two domains; namely, the particle beam optics of the OPPIS and the physical limitations in optical pumping. The beam optics problem is particularly concerned with the extraction system optimization and immersed flow beam dynamics for the ECR source in a 2.5 T magnetic field. Beam diagnostic techniques should be designed and used in the ECR chamber for better understanding of the plasma confinement. Radiation trapping is considered to be an important physical limitation in optical pumping, as higher sodium density is always needed.

Bibliography

[1] Polarized Beams at SSC (Ann Arbor, 1986), AIP Conf. Proc. No. 145, 1986.

[2] KAON Factory Proposal, TRIUMF, 1985.

[3] W. Haeberli, Hel. Phys. Acta. 59 (1986) 513.

[4] P. Schiemenz, Hel. Phys. Acta. 59 (1986) 620.

[5] A.J. Litchtenberg, *Phase-Space Dynamics of Particles*, (Wiley, 1969).

[6] G.G. Ohlsen, J.L. McKibben, R.R. Stevens, Jr and G.P. Lawrence, 73 (1969) 45.

[7] E.K. Zavoiskii, Soviet Physics JETP 5 (1957) 338.

[8] W. Haeberli, Proc. 2nd Int. Sym. Pol. Phenom. in Nucl. React (p. Huber and H. Schopper, eds.) Birkhauser Basel 1966.

[9] G.J. Witteveen, Nucl. Instr. and Meth. 158 (1979) 57.

[10] L.W. Anderson, Nucl. Instr. and Meth. 167 (1979) 363.

[11] P.G. Sona, Energia Nucl. 14 (1967) 295.

[12] C.J. Anderson, A.M. Howald and L.W. Anderson, Nucl. Instr. and Meth. 165 (1979) 583.

[13] J. Uegaki, P.W. Schmor, P. Levy and Y. Mori, Phys. Lett. A 115 (1986) 216.

[14] E.A. Hinds, W.D. Cornelius and R.L. York, Nucl. Instr. and Meth. 189 (1981) 599.

[15] D. Tupa, L.W. Anderson, D.L. Huber and J.E. Lawler, Phys. Rev. *A33* (1986) 1045.

[16] D.R. Swenson and L.W. Anderson, Nucl. Instr. and Meth. *B29* (1988) 627.

[17] M.A. Bouchiat and J. Brossel, Phys. Rev. 147 (1966) 41.

[18] A.N. Zelenskii, S.A. Kokhanovskii, V.M. Lobashev and V.G. Polushkin, Nucl. Instr. and Meth. *A245* (1986) 223.

[19] Y. Mori, K. Ikegami, A. Takagi, S. Fukumoto and W. Cornelius, Nucl. Instr. and Meth. 220 (1984) 264.

[20] D. Tupa and L.W. Anderson, Phys. Rev. A 36 (1987) 2142.

[21] R.W. Carlson, Methods of Experimental Physics, vol. 14: Vacuum Physics and technology; edited by G.C. Weissler and R.W. Carlson, (Academic Press, 1979).

[22] M. Kimura, R.E. Olson and J. Pascale, Phys. Rev. *A26* (1982) 3113.

[23] F. Ebel and E. Salzborn, J. Phys. B: At. Mol. Phys. 20 (1987) 4531.

[24] R. Hultgren, P.D. Desai, D.T. Hankins, M. Gleiser, K.K. Kelley and D.D. Wagman, *Selected values of the thermodynamic properties of the elements*, (American society for Metals, 1973).

[25] A.S. Schlachter, K.R.Stalder and J.W. Stearns, Phys. Rev. *A22* (1980) 2494.

[26] C. Lyneis, in Workshop on the 6th Int. ECR Ion Source, Lawrence Berkeley Lab. Pub-543, 1985.

[27] P.W. Schmor, Hel. Phys. Acta. 59 (1986) 643.

[28] M.J. Jakobson and R.J. Hayden, Nucl. Instr. and Meth. *A258* (1987) 536.

[29] L. Valyi, *Atom and Ion Sources* (Wiley, London, 1977).

[30] K.L. Brown and S.K. Howry, TRANSPORT/360, SLAC report 91, (1970).

[31] A.P. Banford, *The Transport of Charged Particle Beams* (Spon, London, 1966).

[32] T.S. Green, Rep. Prog. Phys. 37 (1974) 1257.

[33] J.R. Coupland and T.S. Green, Nucl. Instr. and Meth. 125 (1975) 197.

[34] C. Lejeune, *Advances in Electronics and Electron Physics, Supplement 13C* (Academic Press, 1983).

[35] P.W. Allison, D.B. Holtkamp and J.D. Sherman, IEEE Trans. $NS-30(4)$ (1983) 2204.

[36] S. Page, private communication on preliminary runs of TRIUMF experiment E497. Also, Univ. of Manitoba Inter. Energy Phys. Prog. Report, 1987-88, p.10.

[37] V. Bargmann, L. Michel and V.L. Telegdi, Phys. Rev. Lett. 2 (1959) 435.

[38] G. Roy, TRIUMF internal report, no. TRI-DNA-72-8, 1972.

[39] C.J. Kost, RELAX3D, a program to solve 2- and 3-Dimensional Poisson and Laplace equations, TRIUMF, 1985.

[40] C.J. Kost, private communication.

[41] Y. Mori, A. Takagi, K. Ikegami, S. Fukumoto, A. Ueno, C.D.P. Levy and P.W. Schmor, Nucl. Instr. and Meth. *A*268 (1988) 270.

Appendix A

Derivation of $P(t)$

In this appendix, the time dependent polarization $P(t)$ of optically pumped sodium atoms is derived in terms of measurable physical quantities in the measurements of sodium $\langle S_z \rangle$ wall relaxation (chapter 3).

The polarization relaxation time T, after the pumping laser beam is chopped off, gives rise to a time dependent angular rotation of the Faraday rotation angle $\theta_p(t)$ of the linear polarization of the probe laser beam (see fig. 3.1). $\theta_p(t)$ is given by

$$\theta_p(t) = \theta_p e^{-t/T} \tag{A.1}$$

where θ_p is the steady state Faraday rotation angle.

The intensity of the transmitted probe laser beam through polarizer ♯2 (fig. 3.1), as measured by the output of the photomultiplier (PMT), is given by

$$S(t) = I_0 sin^2 \theta_p(t) \tag{A.2}$$

where I_0 is the intensity of the incident probe laser beam on the polarizer ♯2, and $\theta_p(t)$ is given by eq.(A.1). Therefore

$$S(t) = I_0 sin^2 \left[\theta_p e^{-t/T}\right] \tag{A.3}$$

Solve eq.(A.3) for $e^{-t/T}$,

$$e^{-t/T} = \frac{1}{\theta_p} sin^{-1} \sqrt{\frac{S(t)}{I_0}} \tag{A.4}$$

The time dependent polarization $P(t)$ during relaxation is exponentially given by

$$P(t) = P_0 e^{-t/T} \tag{A.5}$$

where P_0 is the steady state $\langle S_z \rangle$ polarization of sodium atoms achieved by optical pumping.

Substituting $e^{-t/T}$ from eq.(A.4) into eq.(A.5), $P(t)$ becomes

$$P(t) = \frac{P_0}{\theta_p} sin^{-1} \sqrt{\frac{S(t)}{I_0}}. \tag{A.6}$$

The quantity I_0 can be obtained by relating the steady state PMT signal from the oscilloscope traces and the steady state Faraday rotation angles as follows.

At steady state, $t = 0$, from eq.(A.2)

$$S(0) = I_0 sin^2 \theta_p \tag{A.7}$$

where $S(0)$ is the PMT signal at the instant when the pumping beam is off (see fig. A.1). Therefore

$$I_0 = \frac{S(0)}{sin^2 \theta_p}. \tag{A.8}$$

Substituting I_0 from eq.(A.8) into eq.(A.6),

$$P(t) = \frac{P_0}{\theta_p} sin^{-1} \left[\frac{S(t)}{S(0)} sin^2(\theta_p) \right]^{1/2}, \tag{A.9}$$

which is eq.(3.3) in chapter 3.

Therefore the time dependent polarization $P(t)$ during relaxation can be obtained directly from the measurable quantities P_0, θ_p and the PMT output.

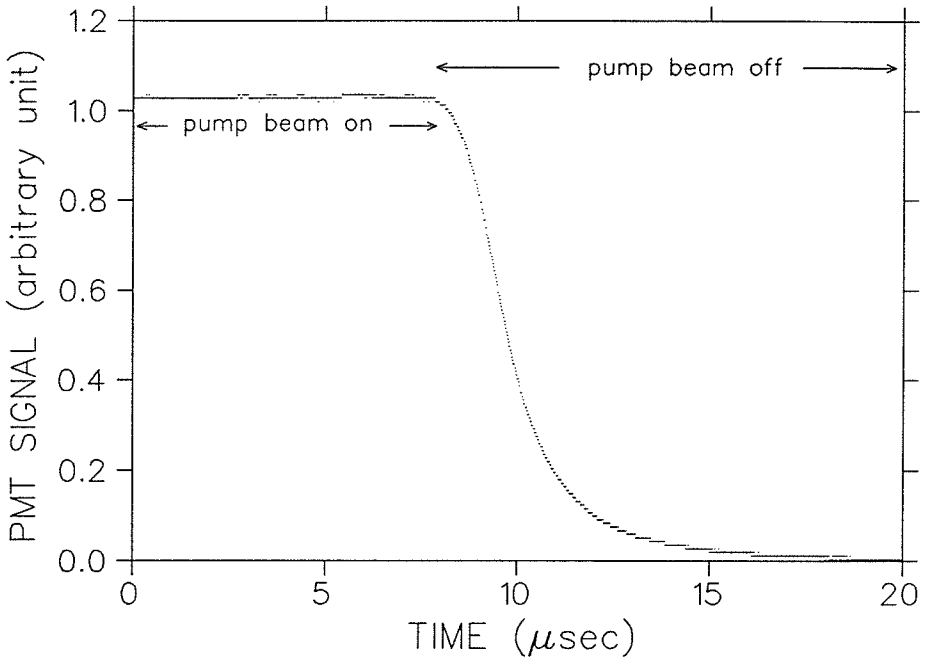

Figure A.1: Example of a photomultiplier (PMT) signal.